J. Fluid Mech. (1994), *vol.* 279, *pp.* 313–350

Instantaneous three-dimensional concentration measurements in the self-similar region of a round high-Schmidt-number jet

By M. YODA[1]†, L. HESSELINK[2] AND M. G. MUNGAL[3]

[1] Department of Aeronautics and Astronautics, Stanford University

[2]Departments of Aero. and Astro. and Electrical Engineering, Stanford University

[3] Mechanical Engineering Department, Stanford University, Stanford, CA 94305, USA

(Received 21 September 1992 and in revised form 13 June)

The virtually instantaneous three-dimensional concentration fields in the self-similar region of natural or unexcited, circularly excited and weakly buoyant round jets of Reynolds number based on nozzle diameter of 1000 to 4000 are measured experimentally at a spatial resolution of the order of the Kolmogorov length scale. Isoconcentration surfaces are extracted from the concentration field. These surfaces along with their geometrical parameters are used to deduce the structure and modal composition of the jet. The concentration gradient field is calculated, and its local topology is classified using critical-point concepts.

Large-scale structure is evident in the form of 'clumps' of higher-concentration jet fluid. The structure, which has a downstream extent of about the local jet diameter, is roughly axisymmetric with a conical downstream end. This structure appears to be present only in fully turbulent jets. The antisymmetric two-dimensional images previously thought to be axial slices of an expanding spiral turn out in our data to instead be slices of a simple sinusoid in three dimensions. This result suggests that the helical mode, when present, is in the form of a pair of counter-rotating spirals, or that the $+1$ and -1 modes are simultaneously present in the flow, with their relative phase set by initial conditions.

In terms of local structure, regions with a large magnitude in concentration gradient are shown to have a local topology which is roughly axisymmetric and compressed along the axis of symmetry. Such regions, which would be locally planar and sheet-like, may correspond to the superposition of several of the layer-like structures which are the basic structure of the fine-scale passive scalar field (Buch & Dahm 1991; Ruetsch & Maxey 1991).

1. Introduction

The search for organized or coherent structure in turbulent shear flows has been a field of great interest for the last two decades (Cantwell 1981; Fiedler 1988). Although many researchers have shown that large-scale or coherent structure exists in the far-field region of planar free mixing layers and plays a significant role in their mixing (Brown & Roshko 1974; Fiedler 1974; Breidenthal 1981), a similar description for

† Present address: Woodruff School of Mechanical Engineering, Georgia Institute of Technology, Atlanta, GA, USA.

the self-similar region of its three-dimensional analogue, the round jet, has yet to be well-established.

It has been experimentally known for at least twenty years that the near field of a round jet is an axisymmetric mixing layer, dominated by vortex rings generated by the Kelvin–Helmholtz instability (Bradshaw, Ferriss & Johnson 1964; Crow & Champagne 1971). These axisymmetric vortex rings were thought to be a manifestation of the dominant axisymmetric mode predicted by linearized stability theory (Batchelor & Gill 1962; Michalke 1971). In the far field of the jet, however, classical integral visualization methods such as shadowgraphy and schlieren showed a nearly homogeneous turbulent flow dominated by small spatial scales. This result led to a model of the jet consisting of a train of vortex rings in the near field which were then broken down into progressively smaller spatial scales as they were convected downstream.

In 1983, Dimotakis, Miake-Lye & Papantoniou visualized an internal axial 'slice' of the far field of a water jet using the laser-induced fluorescence (LIF) technique at Reynolds numbers ranging from 650 to 10000. Their two-dimensional instantaneous axial images of the jet concentration field were radically different from the traditional model: the flow was spatially inhomogeneous, with eddies (regions of approximately constant concentration) of a dimension comparable to the local jet diameter. Two morphologies were observed in these axial slices: the jet had either a roughly antisymmetric (zigzag), or symmetric, outline with respect to its axis.

The large-scale structure of both gaseous and liquid jets has since been the subject of several investigations (Dowling & Dimotakis 1990; Dahm & Dimotakis 1990). In many of these studies, conclusions are drawn about the far-field structure of the jet from a series of two-dimensional axial slices of an inherently three-dimensional flow. In liquid jets, Prasad & Sreenivasan (1990) were the first (to our knowledge) to measure the virtually instantaneous three-dimensional concentration field in the transitional region of a turbulent round jet, but their measurements suffered from low out-of-plane spatial resolution (about 100 times their Kolmogorov scale) and weak signal. Recently, Dahm, Southerland & Buch (1991) have resolved the Batchelor scale with their four-dimensional (space plus time) concentration measurements in the far field of a coflowing jet, but they have had to sacrifice the overall picture in order to fully resolve the diffusion-limited length scales.

In addition to investigating the large-scale structure, a three-dimensional concentration measurement presents us with a new possibility to detect the modes predicted by Batchelor & Gill (1962) and Michalke (1971) for the mean velocity field. Linearized stability analyses of the round jet have shown for normal (e.g. axisymmetric, helical and double helical) mode disturbances that the most unstable or rapidly growing perturbation on a typical far-field Gaussian mean velocity profile is the helical, or $|n| = 1$, mode. From this result, it was concluded that the helical mode would be dominant in the far field.

Although several experimental studies (Mattingly & Chang 1974; Strange & Crighton 1983; Petersen, Samet & Long 1988) have confirmed the existence of the helical mode based upon multipoint velocity measurements in the near field of both natural and excited jets, Tso & Hussain (1989) are to our knowledge the only researchers to search for this mode in the far field. They concluded from preconditioned multipoint velocity measurements in a $Re = 6.9 \times 10^4$ air jet that the helical mode was about four times as common as the next most common axisymmetric mode.

This helical mode must determine or 'shape' the large-scale structure of the far field of the jet, similarly to the near field, where the vortex rings are thought to arise from the dominant axisymmetric mode. It must also shape the large-scale patterns of a passive tracer convected by this (mean) velocity field, or what we would see in a visualization of the turbulent jet. Based upon the antisymmetric shapes seen in their planar visualizations, Dimotakis *et al.* (1983) proposed that the far field of the jet in three-dimensional flow visualizations would then be in the form of an 'expanding spiral' (an axial two-dimensional slice of a spiral would then be an antisymmetric zigzag).

In this study, we make the assumption when attempting to identify these predicted modes in the concentration field that the large-scale structural 'patterns' in the concentration field are shaped by the helical mode (although precisely how this is achieved is unclear). It is therefore assumed after Dimotakis *et al.* (1983) that the far field of this flow is in the form of an expanding spiral, and the three-dimensional datasets shown here are deliberately biased: only those which show clearly antisymmetric shapes with respect to the jet axis are analysed. To further enhance our chances of detecting the supposedly dominant helical mode in the far field, circularly forced as well as natural jets are investigated.

The volume of data that can be recorded and analysed is still limited by present technology. Given this limitation and our interest in large-scale structure, we chose to acquire data at a spatial resolution of about the Kolmogorov scale over the full extent of the flow. The concentration measurements presented here are therefore under-resolved by two orders of magnitude in comparison with the diffusion-limited or Batchelor length scale. As such, these results complement the results of Dahm *et al.* (1991), who have fully spatially resolved the concentration field over a small piece of the flow (10% of their flow width).

Furthermore, data of this type are also limited by our ability to acquire, store and process data in terms of the simple number of independent realizations. Results from eight datasets (out of a total of 30) are presented here. Although this is certainly much too small a number to obtain adequate statistics of the flow (cf. § 3.1), conclusions can still be drawn in terms of qualitative larger-scale structural features, much like the work of Buch & Dahm (1991), who characterized the fine structure of the passive scalar field from five independent datasets. Results from planar flow visualizations over time (Yoda, Hesselink & Mungal 1992) implied that the large-scale structure in the flow was robust and common enough to be evident even in this limited number of realizations.

Despite these limitations, the data still represent a significant advance over previous large-scale measurements, since they are (to our knowledge) the first three-dimensional concentration field measurements over the entire flow width at even this spatial resolution. The results presented here should therefore be seen as a first attempt to characterize and classify the three-dimensional structure in the far field of the jet. We use the data to investigate the instantaneous three-dimensional large-scale structure in the far field of the jet, and how the dominant helical mode predicted by stability theory 'shapes' this structure. The concentration gradient, which represents the flux of passive scalar, is calculated, and its local topology is investigated using critical-point concepts.

Jets at Reynolds number 1000 to 4000 are investigated over distances of 30 to 83 nozzle diameters downstream, corresponding to 2 to 4 local jet widths. Three-dimensional concentration measurements are obtained using the quantitative laser-induced fluorescence (LIF) technique and a rapidly scanned laser light sheet. Section 2

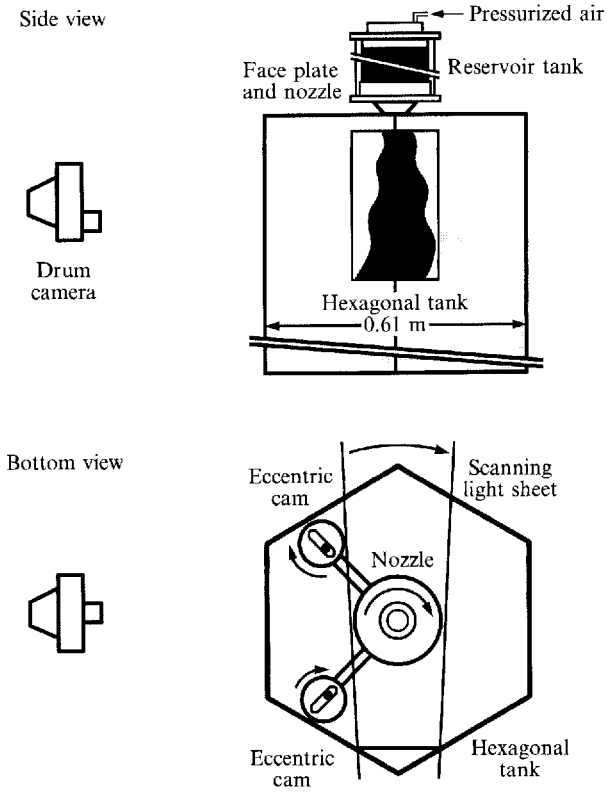

FIGURE 1. Schematic of the flow facility. Pressurized air drives the dyed jet fluid into tank of still undyed water. The flow is illuminated by a pulsed laser light sheet scanned over an angle of 4° across the jet width, and the resultant laser-induced fluorescence is imaged onto film by a high-speed camera. Two perpendicular eccentric cams are used to circularly excite the jet by moving the nozzle in a circular orbit.

describes the data acquisition methods and the characterization of the flow. Section 3 starts with a discussion of the limitations of the data. Based upon these limitations, the choice of the two relatively simple analysis methods used in this work are described and discussed. The concentration data are visualized and analysed by displaying three-dimensional isoconcentration surfaces and calculating some simple geometric parameters, respectively. We then calculate the concentration gradient field and analyze its topology using critical-point concepts. Section 4 presents and discusses our results. Our most unexpected result is that the far field of the turbulent round jet appears not to be in the form of an expanding spiral, but instead in the form of a *pair* of counter-rotating spirals, implying that the +1 and −1 helical modes are present simultaneously in this flow.

2. Experimental details

2.1. *Flow facility*

The flow investigated here is a round water jet with Reynolds numbers based on the nozzle diameter d_o of Re=1000, 2000 and 4000. Since the mean turbulent 'flame length' becomes independent of Re above 3000 (Dahm, Dimotakis & Broadwell 1984), the highest Re flow should be representative of turbulent jets, while the two lower Re

cases should be similar to the transitional *Re* cases studied by Dimotakis *et al.* (1983). The flow facility, illustrated in figure 1, is described in more detail in Yoda (1992). Pressurized air drives 80 μmol disodium fluorescein (Schmidt number $Sc = 2075$, from Buch & Dahm 1991) from a cylindrical reservoir tank through a honeycomb to eliminate swirl out of a nozzle ($d_o = 0.48$ cm) into a hexagonal tank of clear water 61 cm across and 100 cm deep. The jet nozzle (designed and built by W. C. Reynolds) is forced circularly with a variable-speed motor at a non-dimensionalized frequency or Strouhal number $St = 0.3$. The amplitude of the forcing is the maximum possible with the apparatus (about $0.3d_o$).

In the experiments the ambient fluid is always slightly warmer than the jet fluid (by at least 1°C), and so negative buoyancy will eventually dominate the flow. The portion of the flow which is momentum-driven can however be estimated using the following argument: if stratification in the ambient fluid is negligible ($< 1°C\ m^{-1}$ in the experiments), the ceiling height† x_m of the negatively buoyant jet can be measured as a function of the temperature differential between the jet and ambient fluids, and the results of Turner (1966):

$$x_m = 1.85\ Fr\, d_o, \tag{2.1}$$

can be used to obtain an estimate of the Froude number *Fr*.

The characteristic length scale describing the relative importance of momentum and buoyant fluxes (M and B, respectively), l_M, is then (Papanicolau & List 1988)

$$l_M = \frac{M^{3/4}}{B^{1/2}} = \left(\frac{\pi}{4}\right)^{1/4} Fr \left(\frac{\rho_o}{\rho_a}\right)^{1/4}. \tag{2.2}$$

ρ_o and ρ_a are the jet and ambient fluid densities, respectively. Papanicolau & List found in their experiments on buoyant jets that in the region $x'/l_M < 1$, where x' is the downstream distance from the virtual origin, the flow was momentum-dominated. Chen & Rodi (1980) suggest from their review of experimental data a more stringent criterion for the region of the flow which is non-buoyant or momentum-driven:‡

$$\frac{x'}{l_M} < 0.5; \tag{2.3}$$

this criterion was met in these experiments. Buoyancy effects are essentially negligible at the two higher *Re* investigated (2000 and 4000) for temperature differentials of up to 5°C, but they are quite significant at $Re = 1000$.

In our region of interest, the dyed jet fluid should be mixed with at least twice as much ambient fluid from the arguments presented in the far-field mixing model of Broadwell (1989) and Dahm *et al.* (1984), and therefore the dye must be significantly colder than the ambient fluid to achieve momentum-dominated flow in the far field. We present here data from both buoyancy-tainted ($Fr \approx 100$, based on (2.1)) and momentum-driven jets at this *Re*. This weakly negatively buoyant case is referred to in this paper as the 'buoyant' jet.

2.2. *Data acquisition*

The flow is illuminated parallel to the jet axis from the side with a light sheet about 1.5 mm thick from a 20 W copper vapour laser (MetaLaser Model 251) pulsed at

† The ceiling height of a negatively buoyant jet is the maximum height (or depth) that the jet reaches before reversing flow.

‡ A factor of $(\pi/4)^{1/4}$ is ignored in this formulation (cf. Dowling 1988).

10 kHz. The relatively thick sheet has a Rayleigh range slightly greater than the region of interest (17 cm along the radial y-direction) and spreads slightly (2%) along the downstream dimension (x, measured from the jet nozzle exit) as it propagates through the flow. A rotating mirror scans the pulsed light sheet across the jet width (Figure 1). The total radial scan angle is very small (4°), resulting in virtually parallel slices of the concentration field. The light sheet illuminates the region $30d_o \leqslant x \leqslant 83d_o$, corresponding to two to four local jet widths (local jet width $\delta(x') = 0.44x'$) in the far field of the jet. This region is beyond the minimum far-field location of $x' = 20d_o$ recommended by Dowling & Dimotakis (1990) based on self-similarity of the mean concentration field.

The 511 nm (green) line of the copper vapour laser excites fluorescence from the fluorescein in the jet fluid. Note that the maximum concentration of dye in the region of interest should be no more than one-third of the initial pure jet fluid concentration of 80 μmol, or 27 μmol at the farthest upstream location, $x/d_o = 30$. Our experimental calibrations verify the linear response of fluorescein (Koochesfahani & Dimotakis 1986) excited at this wavelength for our range of dye concentrations and for the light intensities used in the experiments (the maximum light exposure incident on the dye $\mathscr{E}_{max}$ is of the order of 0.5 mJ cm^{-2}). Furthermore, the effects of laser light attenuation are negligible in the data – in other words, there is little detectable decay in signal in our mean concentration profiles (Figure 4) as the laser light sheet propagates through the flow.

The images of fluorescence intensity are recorded at virtually normal incidence by a high-speed drum camera (Cordin Dynafax Model 350) converted to a streak camera with a Nikon f/1.2 50mm focal length lens. The data are acquired at 10^4 Hz (i.e. each laser pulse frames a single image) on 35 mm Kodak TMax 3200 film push-processed to ASA 12500. Because the camera has a limited film capacity, we are limited to acquiring one dataset of 100 pictures per jet run. The photographs are taken through an orange filter (Kodak Wratten No. 15), which admits only the red-shifted fluorescence.

In all runs we wait at least twice the time t_o for the jet front to reach the farthest downstream location of interest ($t_o(x) = x^2/(12.4\nu Re)$, where ν is the kinematic viscosity) after jet startup before acquiring data to ensure fully developed flow. The instantaneous three-dimensional data are also acquired before the jet front reaches the bottom of the tank, to avoid floor effects.

This technique gives us x-y slices of the jet at different z-locations and different times. If however the data are acquired over a period of time which is so brief that no fluid element has been convected more than the minimum spatial resolution, we can say that the data are effectively instantaneous. The individual slice exposure of 30–40 ns (= laser pulse length of 30 ns plus the additional fluorescence decay time of a few ns) is brief enough to freeze the flow within a slice. In addition, a fluid element will travel at most 1.7 mm (for $Re = 4000$, $y = z = 0$, $x/d_o = 30$) downstream over the total data acquisition time of 10 ms (maximum of 100 images at 10 kHz). The spatial resolution is limited to the spacing between the x-y slices of 1.7 mm. The data are therefore effectively instantaneous to within our spatial resolution.

To obtain the fluorescent dye (and therefore jet fluid) concentration, the light sheet profile must be directly measured in addition to the fluorescent intensity. To accomplish this, the light sheet is photographed as it propagates through a test cell filled with recirculating (to avoid photobleaching) 10 μmol fluorescein. The beam profile is stable to within a few percent during a single laser run, and so only one light-sheet profile calibration is performed per laser run. These measurements are

acquired on the same film as the jet slices using an identical camera lens and filter, and are converted back to light intensity using the procedure described in the following paragraphs. From these measurements of the light-sheet profile, we estimate that the maximum error inherent in our data acquisition system is about $\pm 7\%$, corresponding to a r.m.s. error of $\pm 5\%$.

The images (both jet data and light-sheet profiles) are digitized by a scanning microdensitometer (Perkin-Elmer PDS Model 1010GM) into two-dimensional arrays of optical density D at 12 bits per pixel. They are then downloaded to a Silicon Graphics Iris workstation (Model 4D/220GTX), median filtered over a 5×5 window to remove small isolated defects and artifacts and are converted to fluorescent light intensity on the film using the relation (Goodman 1968)

$$D - D_o = -\log_{10}(T/T_o) = \gamma \log_{10}(\mathscr{I}t)\,, \tag{2.4}$$

where D is the optical density of the developed negative, D_o is the gross fog optical density of the film (set by the digitization calibration to zero), T and T_o are the transmission (in percent) of the image and its background, respectively, $\mathscr{I}$ is the light intensity incident on the film, and t is the time over which the film is exposed. The γ-value of the film under our developing conditions is experimentally determined to be 1.04. After push processing the film to an ASA of 12500, calibrations (Yoda 1992) showed that for $D > 0.6$, the film obeyed (2.4) to within 5%. This film grain noise appears to be the major source of error in the data.

Finally, the set of two-dimensional images of fluorescent intensity in the jet are divided by the appropriate light-sheet profile to obtain the passive scalar concentration field of the jet. The images are then rescaled to 8 bits per pixel (255 grey scales) and stacked into an x-y-z array. Note in these experiments that we have only the *relative* concentration in this region of the flow. All concentrations will therefore be reported in this paper as a percentage value of the maximum instantaneous concentration seen in the region of interest.

2.3. *Characterization of the flow*

In order to characterize the flow, measurements were taken of both the mean velocity profile at the jet nozzle and the mean concentration field along the jet axis. The velocity profile at the jet nozzle is measured using a low-density particle tracking technique, or particle tracking velocimetry (PTV) (Adrian 1986). A 2 mm thick light sheet from a copper vapour laser pulsed at 200–800 Hz illuminates the jet, which is seeded with 40 μm diameter alumina particles (seeding density ≈ 30 particles ml^{-1} of pure jet fluid). Up to a dozen pictures of the seeded jet are taken over six pulses of the laser, during which the flow moves $1.5d_o$, and the velocity is obtained by measuring the particle displacement over three to five laser pulses. Since the flow at the nozzle is steady, a composite velocity profile can be built up from several PTV pictures. The relatively thick (2 mm) light sheet ensures that a reasonable number of particles remain visible in the sheet over the exposure interval.

Figure 2 shows the velocity profile obtained with this technique for the three Reynolds numbers studied. In all cases the particle tracks used to obtain the velocity profile are taken within one nozzle diameter of the nozzle exit. As can be seen in the figure, the velocity profile is symmetric and level in the centre of the nozzle, with the boundary-layer thickness increasing as Re decreases. We approximate the boundary-layer velocity profile in this figure with a (half) Gaussian (Mattingly & Chang 1974). Using these fitted velocity profiles, we can calculate the jet momentum and mass fluxes (J_o and $\dot{m}_o$, respectively) and use these quantities to define a momentum-based

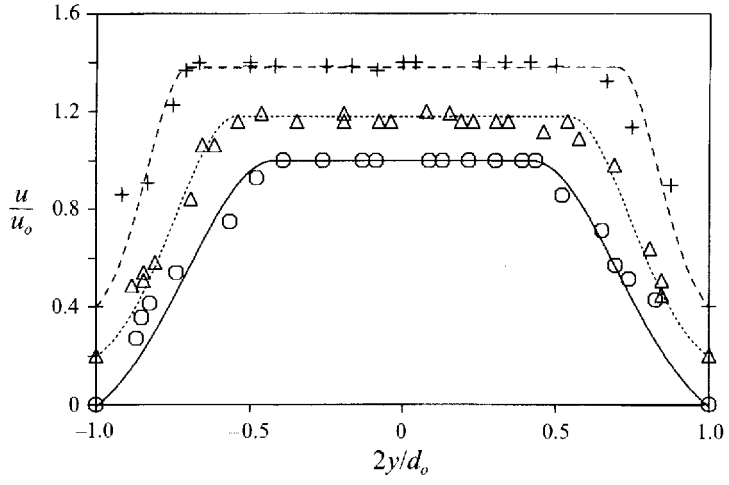

FIGURE 2. Normalized velocity profiles (u/u_o *vs.* $2y/d_o$) of the flow out the jet nozzle measured with PTV for $Re = 1000$ (circles), 2000 (triangles; vertically offset 0.2 units), and 4000 (plusses; vertically offset 0.4 units). A horizontal line has been drawn across the top-hat part of the curve and a (half) Gaussian has been fitted to the sides of the profile (Mattingly & Chang 1974). In all cases the points used to obtain these values were taken within d_o of the nozzle exit.

effective jet source velocity U_s and diameter d^* (Becker & Yamazaki 1978; Dahm & Dimotakis 1987):

$$U_s = \frac{J_o}{\dot{m}_o} \; ; \quad d^* = \frac{2\dot{m}_o}{(\pi\rho_o J_o)^{1/2}} \, . \tag{2.5}$$

These quantities can then be used to define the momentum-based Reynolds number Re^*:

$$Re^* = \frac{U_s d^*}{\nu} \, . \tag{2.6}$$

Re^* is related to Re, to the Reynolds number based upon the nozzle diameter d_o and the velocity that would be expected from the measured mass flux at the nozzle and a top-hat velocity profile U_o, as follows:

$$Re^* = Re\frac{d_o}{d^*} \, . \tag{2.7}$$

$Re = 4000$ therefore corresponds to $Re^* = 4400$ ($d^*/d_o = 0.90$), $Re = 2000$ corresponds to $Re^* = 2300$ ($d^*/d_o = 0.86$), and $Re = 1000$ corresponds to $Re^* = 1200$ ($d^*/d_o = 0.83$). Given these relatively minor differences between the flow parameters based upon initial flow conditions (d_o and U_o) and those based upon the momentum and mass fluxes (J_o and $\dot{m}_o$), the results presented here are non-dimensionalized with respect to initial flow conditions.

The mean concentration field is obtained by taking time exposures of the flow over 10–20 local passage times (local passage time $\tau = \delta(x')/U_c(x')$, where $U_c(x') = 6.2\nu Re/x'$ is the local centreline velocity and $x = 83d_o$). Recirculation from the jet hitting the bottom of the ambient fluid tank makes it impossible to take data over longer periods; this relatively short averaging time is the largest source of the error of about 8% in the measurements. The averages are acquired on Kodak Ektar 25 film

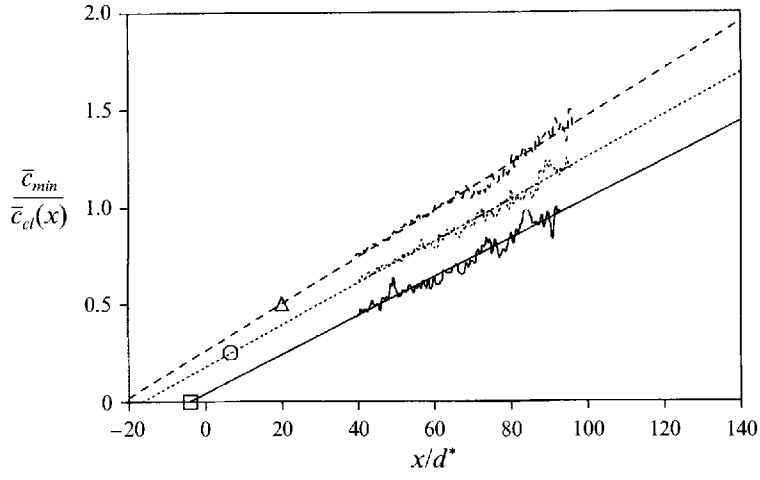

FIGURE 3. The streamwise evolution of the mean jet centerline concentration. The normalized inverse of the centerline concentration $\bar{c}_{min}/\bar{c}_{cl}(x)$ is plotted *vs.* the downstream distance in jet momentum diameters (x/d^*) for the $Re = 4000$ (solid line), 2000 (dotted line; vertically offset 0.2 units) and 1000 (dashed line; vertically offset 0.4 units) natural jets. The straight lines are fitted to the data with linear regression. The virtual origins of the $Re = 4000$, 2000, and 1000 jets are indicated by the square, circle and triangle, respectively.

instead of the TMax 3200 used for the instantaneous measurements, because Ektar (unlike TMax) does not suffer from reciprocity failure, even over exposure times of several hundred seconds (Eastman 1991).

From similarity considerations, the mean concentration on the centreline $\bar{c}_{cl}(x)$ should decay as $1/x'$ (Chen & Rodi 1980):

$$\frac{\bar{c}_{cl}(x)}{c_o} \propto \frac{d^*}{x'} \mathscr{F}(\eta)\,, \tag{2.8}$$

where c_o is the concentration of pure jet fluid and $\eta = (y^2 + z^2)^{1/2}/x'$ is the non-dimensionalized radial coordinate. After processing the images as described above to obtain the true concentration field, the location of the virtual origin $x = x_o$ (note $x' = x - x_o$) should be where the curve $1/\bar{c}_{cl}(x)$ *vs.* x intersects the horizontal axis. Figure 3 is the graph of $\bar{c}_{min}/\bar{c}_{cl}(x)$ ($\bar{c}_{min}$ = the minimum mean concentration) *vs.* the non-dimensionalized downstream coordinate x/d^* for the three natural jet cases. The location of the virtual origin x_o moves downstream with respect to the jet nozzle location as Re decreases ($x_o = 3.6d_o$ for $Re = 4000$, $5.7d_o$ for $Re = 2000$, and $16.6d_o$ for $Re = 1000$). As expected, the slopes of these curves are not identical, since only the case at the highest Re of 4000 is self-similar in mean concentration.

Figure 4 shows the mean concentration for a fixed x-location normalized by its value on the centreline $\bar{c}(x,\eta)/\bar{c}_{cl}(x)$ *vs.* the non-dimensional radial coordinate η. In all cases, the radial concentration profile is symmetric and roughly self-similar, in agreement with (2.8). We have made no attempt to fit our data to a Gaussian profile (Chen & Rodi 1980), since again only the highest Re data are self-similar. Our measurements of the spreading rate $\delta(x')/x'$ for these three different Re are all within 10% of each other and the commonly accepted value of 0.44, or a 25° angle. These downstream and radial mean concentration profiles verify the accuracy and validity of the LIF technique and show that our jet behaves normally in time average.

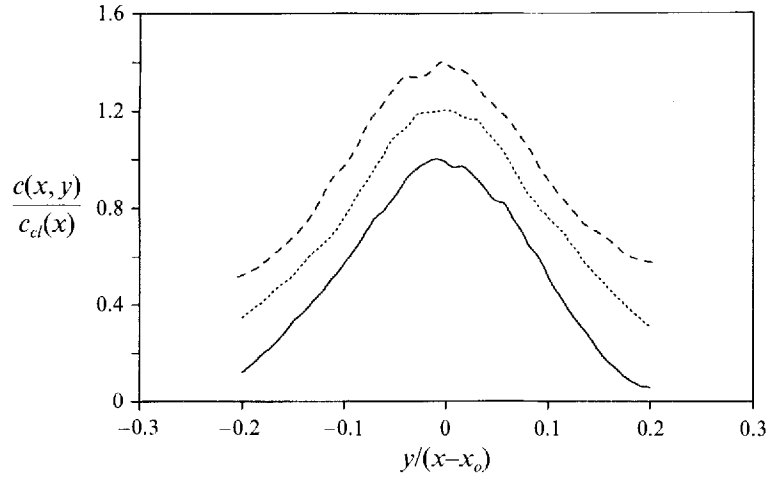

FIGURE 4. Radial mean concentration profiles. The normalized mean concentration ($\bar{c}(x,y)/\bar{c}_{cl}(x)$) is plotted *vs.* the non-dimensionalized radial coordinate ($y/(x-x_o)$, $y = 0$ corresponds to the centreline) for the $Re = 4000$ (solid line), $Re = 2000$ (dotted line; vertically offset 0.2 units) and Re=1000 (dashed line; vertically offset 0.4 units) natural jets. Each of these radial profiles is the average of several profiles at different x-locations in non-dimensionalized coordinates.

We attempted to measure means for the circularly forced and buoyant jets, but it was impossible to acquire an average over even a few local passage times because the enhanced spreading rate of these cases causes the flow to hit the walls of the hexagonal tank shortly after startup, resulting in severe recirculation. We are therefore unable to report either a spreading rate measurement or a measurement of the mean concentration for these cases, but our results indicate that the concentration decay on the centreline of all three different-Re circularly excited jets is very similar in shape. Given our inability to measure a virtual origin, and the uncertainty of whether the circularly excited jet even follows the scaling laws for the natural jet, the location of the virtual origin is simply defined at the nozzle for these cases ($x_o \equiv 0$).

3. Data analysis

3.1. *Data acquisition limitations*

Although the methods described in the previous Section give effectively instantaneous three-dimensional measurements of the passive scalar concentration field, the requirements to achieve 'instantaneous' data and the limitations imposed by present technology in terms of data acquisition speed limit us to a spatial resolution of about 1% of the maximum jet width, or a spatial resolution size which is far greater than the diffusion-limited length scales. Furthermore, the sheer volume of data to be digitized and analysed limits us to just a few realizations of the three-dimensional concentration field, or an inadequate number of realizations for statistical calculations. In this section the requirements for spatially well-resolved data and a statistically representative number of realizations are presented, and the sorts of conclusions which can then be drawn from the data are discussed.

Ideally, concentration measurements should resolve the smallest diffusion length scale in the flow, or the Batchelor scale

$$\lambda_B = \alpha \frac{\delta(x')}{Re^{3/4} Sc^{1/2}} . \tag{3.1}$$

The constant of proportionality α is taken to be about 11 based on the measurements of Buch & Dahm (1991), giving a λ_B of 31 μm for our worst-case conditions at $Re = 4000$ and $x/d_o = 30$.

In order to investigate the large-scale structure in the jet, the flow should be investigated over its entire width and at least a few local widths in the downstream dimension. Even if it were technologically feasible to obtain measurements over such dimensions with a resolution of λ_B, the amount of data that would result from a single such three-dimensional measurement would be about 4 TBytes, or 4×10^{12} Bytes – a data volume which would be impossible to record, much less analyse. Spatial resolution is therefore sacrificed in favour of an overall picture of the large-scale structure of the flow. The spatial resolution here of 1.7 mm is about 50 times this diffusion-limited scale, implying that the concentration measurements are under-resolved by about two orders of magnitude.

The spatial resolution is therefore of the order of the Kolmogorov scale λ_K

$$\lambda_K = \alpha \frac{\delta(x')}{Re^{3/4}} , \tag{3.2}$$

about 1.4 mm for the worst-case conditions above. The spatial resolution is fixed in physical space, and therefore becomes progressively better in terms of the local length scales (which increase with the local jet diameter $\delta(x')$) as we progress downstream.

We would also ideally like to acquire enough independent realizations of the concentration field to have a statistically representative picture of the flow structure. The number of independent realizations required to obtain a good statistical representation of the flow can be estimated using standard methods (Mendenhall, Scheaffer & Wackerly 1986, for example). For n (where n is large) concentration samples from a random set of values with a standard deviation of σ, the magnitude of the error μ expected in the mean concentration value can be estimated by

$$\mu = 2\left(\frac{\sigma}{n^{1/2}}\right) . \tag{3.3}$$

Dowling & Dimotakis (1990) have reported a σ from concentration measurements in gaseous jets of about 22%. A dataset of about 80 realizations is therefore required to estimate the mean concentration field to within an accuracy of ±5% – a data volume of about 320 MByte at even this intermediate spatial resolution.

Up to six independent realizations of each case (different experimental runs) were acquired, but results from only two realizations of the Re=4000 natural jet and one realization of all other cases are presented in § 4 owing to the large volume of data required by even this moderate spatial resolution (about 4 MByte per realization) and the significant amount of time and work required to process and analyse even a single realization. The data are therefore inappropriate for the calculation of statistics.

So what can be learned from our three-dimensional concentration data, given the limits discussed above? We cannot resolve the fine-scale diffusion and mixing processes reported by Dahm *et al.* (1991), but the data are certainly appropriate for investigating the large-scale structure and instability modes present in the flow. Note that the data here are comparable in spatial resolution with those of other researchers who have investigated large-scale structure in two-dimensional studies (Dimotakis *et al.* 1983; Dahm & Dimotakis 1990).

In addition, the concentration gradient field, which represents the flux of the passive

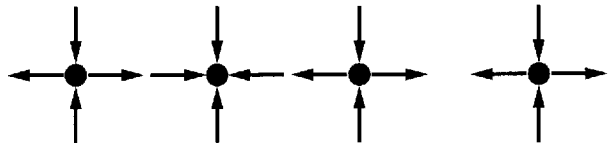

FIGURE 5. (*a*) An attracting node in a plane flanked by two saddle points. (*b*) At a lower spatial resolution, the three critical points in (*a*) appear to be a single saddle point.

scalar, can be calculated from the data. Owing to the limited spatial resolution, we cannot investigate the scalar dissipation or the isotropy of the concentration gradient field. We can however investigate the topology of this field, since the topology of the spatially under-resolved concentration gradient field must remain consistent with that of the fully resolved field. As an illustration, consider the situation in two dimensions of an attracting node between a pair of saddle points (Figure 5*a*). As the spatial resolution becomes worse, these three critical points will 'blur', and become a single saddle point (Figure 5*b*). At this spatial resolution, the specific number of critical points or their types cannot be resolved, but the general qualitative behaviour of the concentration gradient field – that is, that the concentration is increasing as one nears the critical point along the y-axis, and decreasing along the x-axis – remains consistent.

Within the context of these limitations, we can therefore still investigate the large-scale structure of both the concentration field and its gradient, which represents the flux of passive scalar. The data are analysed using two general techniques. The concentration data are visualized as isoconcentration surfaces, and analysed by calculating some simple geometric parameters. The topology of the concentration gradient is analysed using critical-point concepts.

3.2. *The concentration field*

The concentration data are visualized both as planar slices of the data volume and as three-dimensional surfaces of constant concentration, or isoconcentration surfaces. In isoconcentration surface visualization, we extract and display the surface which is the boundary surface between concentration values higher and lower than the prescribed threshold value. To follow the large-scale eddies in the flow, the instantaneous concentration data are rescaled by multiplying each concentration value by its distance from the virtual origin x' (van Cruyningen 1990). The rescaled concentration value c is then

$$c(x, y, z) = x' c_u(x, y, z)\,, \tag{3.4}$$

where c_u is the original instantaneous concentration. This self-similar rescaling compensates for the $1/x'$ decay of the mean concentration (cf. (2.8)), and enables us to see a large diffuse eddy at the farthest downstream point in the flow in the same isoconcentration surface as a smaller more concentrated eddy upstream.

A subsampled version of the dataset is then created by uniformly lowpass filtering the original data over a $3\times3\times3$ window (to reduce noise and aliasing) and using every other point of the filtered data. This subsampled dataset will then have a spatial resolution half that of the original data, or 2.8 mm in physical space. Since we are more interested in the qualitative large-scale features of the isovalue surfaces, this subsampled dataset is used for the visualizations to reduce the computational

overhead required. The surfaces are rendered using the Marching Cubes algorithm (Lorensen & Cline 1987) and in-house software written by P. C. Ning (Ning & Hesselink 1991). The algorithm uses linear interpolation to determine a boundary or isoconcentration surface at the specified value and draws a surface consisting of triangles.

In addition, we compute some geometric parameters from the concentration data. All the parameters here are calculated from the median filtered original spatial resolution datasets. The concentration-based centroid coordinates $(\bar{y},\bar{z})$ are calculated as a function of the downstream distance from the nozzle exit x:

$$\bar{y}(x) = \sum_{y} \frac{c(x,y,z)y}{c(x,y,z)}, \quad \bar{z}(x) = \sum_{z} \frac{c(x,y,z)z}{c(x,y,z)}. \tag{3.5}$$

The value of the centroid at the furthest upstream coordinate ($x = 30d_o$) where the jet centre will have deviated the least in the region of interest from the vertical centreline is then subtracted from these coordinates, and the result is divided by the local jet width $\delta(x')$ to obtain the non-dimensionalized radial centroid coordinates (ξ,ζ):

$$\xi(x) = \frac{\bar{y}(x) - \bar{y}(30d_o)}{\delta(x)}, \quad \zeta(x) = \frac{\bar{z}(x) - \bar{z}(30d_o)}{\delta(x)}. \tag{3.6}$$

The area $\mathscr{A}$ inside each concentration contour is calculated as a function of both concentration threshold and downstream distance:

$$\mathscr{A}(c_{th}, x) = N_{pts}(c \geqslant c_{th}, x)\Delta y \Delta z, \tag{3.7}$$

where c_{th} is the threshold concentration, N_{pts} is the number of datapoints in radial cross-section at x that have a concentration value c greater than or equal to c_{th} and Δy and Δz are the sample spacings in the y- and z-directions.

3.3. *The topology of the concentration gradient field*

A more detailed description of the theory presented here and its applications to fluid flows can be found in Chong, Perry & Cantwell (1990). The Maclaurin series expansion of the concentration gradient ∇c around its local origin is

$$\frac{\partial c}{\partial x_i} - \left(\frac{\partial c}{\partial x_i}\right)_o = \{A_{ij}\}_o (x_j - (x_j)_o); \quad A_{ij} \equiv \frac{\partial^2 c}{\partial x_i \partial x_j}, \tag{3.8}$$

where the o subscript refers to the parameter evaluated at the local origin, and [**A**] is the Jacobian matrix of ∇c. At a critical point, the second term on the left-hand side is zero, and this expression reduces to a first-order differential equation, with [**A**] characterizing the local behaviour of ∇c around the critical point.

Critical-point concepts can however be extended by analysing [**A**] at not only the critical points of the concentration field, but at every point in the flow. We are then actually looking at the topology of a modified concentration gradient field, $\nabla c'$ (the left-hand side of (3.8)), which is the deviation of the actual concentration gradient from its neighbouring values, analogous to the curvature of the gradient. If this field varies slowly with respect to the sample spacing, the topology of this modified field will essentially be that of the concentration gradient.

The eigenvalues of $[A]$ satisfy the characteristic equation

$$\lambda^3 + P\lambda^2 + Q\lambda + R = 0, \tag{3.9}$$

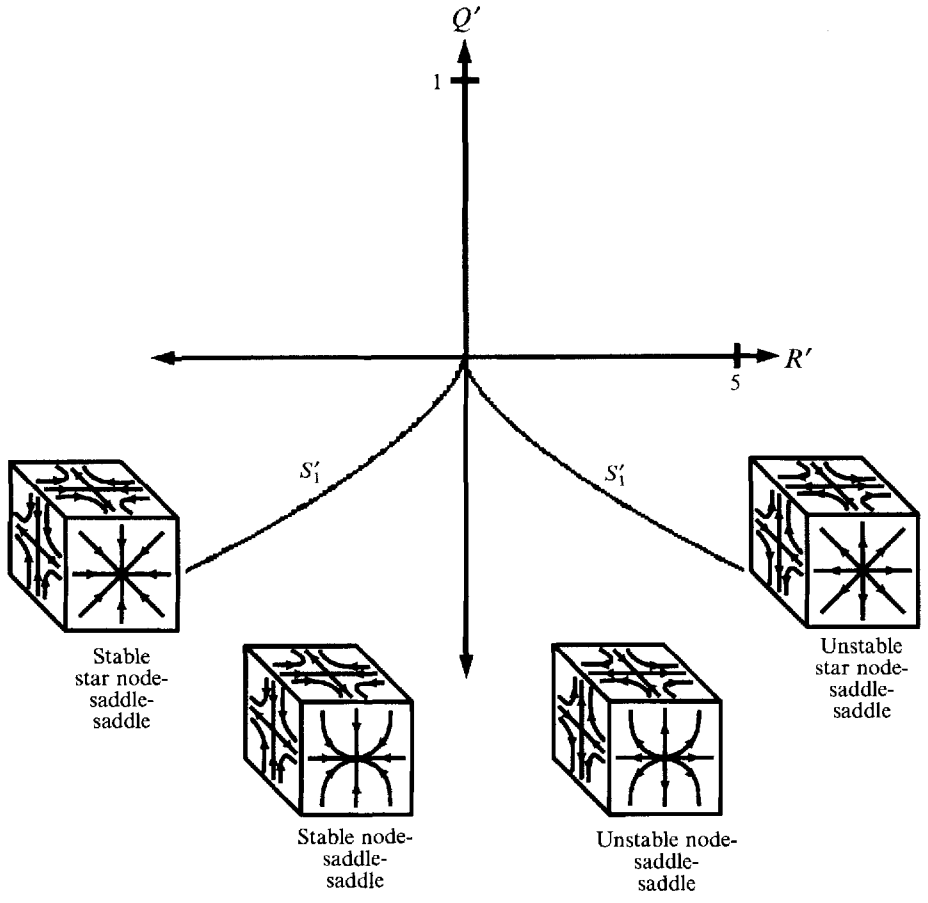

FIGURE 6. The (Q', R')-plane ($P'=0$). Our data lie under the S_1' curve. The R'-axis spans a distance five times that of the Q-axis.

where P, Q and R are the invariants of $[A]$:

$$P = -\text{trace}\,[A]\ ; \quad Q = \frac{1}{2}\left(P^2 - \text{trace}\,[A^2]\right)\ ; \quad R = -\det[A]\,. \tag{3.10}$$

The concentration gradient data can then be compactly displayed as a scatter plot in (P, Q, R)-space – where each vector $\nabla c'$ is represented in this space by the (P, Q, R) of its Jacobian matrix $(A_{ij} = \partial^2 c/\partial x_i \partial x_j)$.

To avoid looking at this three-dimensional space, our results are projected onto the plane $P = 0$ by modifying $[A]$ to make the data trace-free. Since the Jacobian matrix $[A]'$ is symmetric, its eigenvalues will be real, and its invariants (Q', R') will lie under the curve S_1':

$$R' = \pm\frac{2\sqrt{3}}{9}(-Q')^{3/2}\,. \tag{3.11}$$

In this (Q', R')-plane (figure 6), points which lie upon the S_1' curve have two identical eigenvalues (star node-saddle-saddles, in the jargon of Chong *et al.* 1990), implying

that the concentration field corresponding to this point has a locally axisymmetric topology. Points which lie in the right half-plane ($R' > 0$) then correspond to a Jacobian with two positive and one negative eigenvalue (unstable node-saddle-saddles); points which lie in the left half-plane ($R' < 0$) then correspond to a Jacobian with two negative and one positive eigenvalue (stable node-saddle-saddles). And if $R' \approx 0$ (and Q' is large), the datapoint has a two-dimensional topology (i.e. one of the eigenvalues is negligible compared to the other two).

For each datapoint evaluated, the procedure is then as follows: (i) calculate the nine components of its Jacobian matrix, or the second spatial derivatives of the concentration field; (ii) make the Jacobian matrix trace-free by subtracting one-third of the trace of [**A**] from each of the three diagonal matrix elements; (iii) determine the invariants of the modified Jacobian Q' and R'; and (iv) plot the values upon the (Q', R')-plane. The second derivatives of the concentration field are calculated with second-order-accurate central differencing from the lowpass filtered and subsampled concentration field used in the previous section (used to avoid problems with noise when differentiating). The invariants Q' and R' are then calculated and plotted using topological analysis software written by R. Sondergaard (Sondergaard *et al.* 1991). To avoid problems with topological degeneracy in the ambient fluid, where both the concentrations and the concentration gradients are nearly zero, the invariants are calculated only at points where the concentration is greater than 5 out of 255. This entire process of calculating and plotting the invariants takes a few minutes for a plot of 10^5 datapoints.

In addition, the effects of noise on the concentration gradient were investigated by adding randomly generated 'noise' of $\pm 10\%$ maximum concentration (zero mean, or white noise) and 20% (biased noise) to the median filtered original spatial resolution data. After processing the 'noisy' data using the same procedures as those used with the original data – lowpass filtering, and subsampling by a factor of two – (Q', R')-values are calculated and plotted for the 'noisy' data.

The (Q', R')-plots shown in the next Section are not simple scatter plots, but rather plots of contours of the number of points within a unit window of a given (Q', R') location (Soria *et al.* 1994). These modified scatter plots enable us to better visualize the region near the cusp of the curve S_1', where most of the datapoints fall, overlapping and obscuring this region. Contours are shown here going through (Q', R') locations where 1, 10, 100 and 1000 points overlap (to within a unit window); note that a 'contour' through one point is equivalent to a simple scatter plot.

4. Results and discussion

We present in this section results from the concentration field and its gradient. Data are presented for seven different jet cases: (i) the $Re = 4000$ natural jet; (ii) the $Re = 4000$ circularly excited jet ($St = 0.3$); (iii) the $Re = 2000$ natural jet; (iv) the $Re = 2000$ circularly excited jet ($St = 0.3$); (v) the $Re = 1000$ natural jet; (vi) the $Re = 1000$ circularly excited jet ($St = 0.3$); and (vii) the $Re = 1000$ buoyant jet ($Fr \approx 100$). The St (based on d_o) of 0.3 was chosen based on its marked effect on the flow, especially in terms of spreading rate, as seen in the previous x-y-t results (Yoda *et al.* 1992), which also implied that nozzle excitation at this St amplified the antisymmetric large-scale structure.

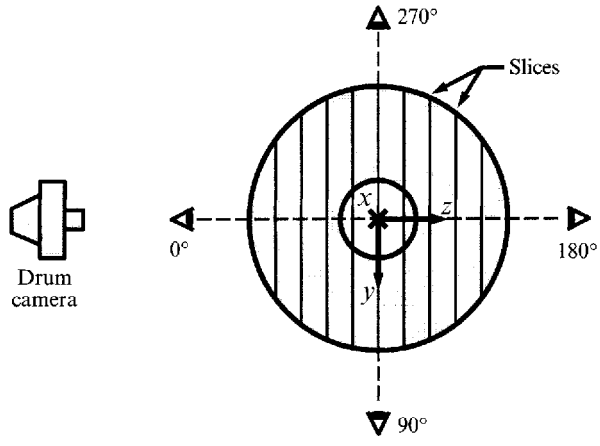

FIGURE 7. Coordinate axes and view orientations for the isoconcentration surfaces. A view of the truncated cone along the flow (x) direction; the small and large circles correspond to the upstream and downstream ends of this cone. The view along which the slices are acquired by the camera is defined as the 0° view.

This St will give a far-field Strouhal number St_f of

$$St_f = \frac{f\delta(x)}{U_c(x)} = 0.071\left(\frac{x}{d_o}\right)^2 St; \quad St = \frac{fd_o}{U_o}, \tag{4.1}$$

where f is the nozzle excitation frequency. For our data, $30 < x/d_o < 83$, corresponding to $St_f = 20$–150. This St_f is certainly too large to excite a single resonant helical mode (W. C. Reynolds 1992, private communication), but the dependence of St_f upon the square of the non-dimensionalized downstream coordinate x/d_o makes it impossible to excite a single mode at any fixed nozzle St for our region of interest.

M. G. Mungal & S. H. Smith (1992, private communication) investigated circularly excited jets in the far field at $0.025 < St < 0.2$, and saw amplification of the helical mode at $St_f = 6.4$, a surprisingly high value given the typical 'preferred' St reported for the near field of the jet. Their result implies that circular excitation at even these high St_f still can couple the helical mode, perhaps through subharmonic or multimodal interactions.

4.1. *The concentration field*

Two realizations of the $Re = 4000$ natural jet and one realization of each of the other cases are shown here. The realizations presented here are those with the most zigzag or antisymmetric two-dimensional slices upon visual inspection. By focusing upon these realizations, we should maximize our chances to see the helical mode.

Two-dimensional projections of the three-dimensional isoconcentration surfaces are presented in this section; the projection orientations are defined in figure 7. In the mean, an isoconcentration surface of the jet from 30–83 nozzle diameters downstream will be a truncated cone. The radial coordinates are y and z; a 0° view of the surface is defined to be along the view direction of the camera, corresponding to an image plane parallel to the original two-dimensional data slices. The 90° and 270° views are then normal views along the y-axis, and the 180° view is the opposite view along the z-axis (these angles refer to rotation about the x-axis). A spiral shape in these surfaces should be evident as an antisymmetric or zigzag outline in these

two-dimensional projections, and the zigzag should be visible along all projection or view angles.

4.2. *Re=4000: natural and circularly excited jets*

Figures 8(*a*) and 8(*b*) show rescaled centreline slices for both the natural (case I) and circularly excited jet (Figures. 8(*c*)–8(*g*) will be discussed subsequently, but are shown here for comparison); these figures correspond to the 0° (cf. figure 7) centreline slice. In these images of the jet fluid concentration, white corresponds to ambient fluid and black corresponds to the maximum jet fluid concentration (darker shades imply higher jet fluid or dye concentration). As expected, circular excitation appears to enhance the width of the jet. Of particular note are the strongly antisymmetric outlines of both the natural and circularly excited jet slices. Our two-dimensional slices look qualitatively similar to those of Dimotakis *et al.* (1983) and Dahm & Dimotakis (1990) at similar *Re*.

Figure 9 depicts isoconcentration surfaces reconstructed from the subsampled versions of the natural jet data at 10, 30, 50 and 80% (of the maximum) threshold concentrations at an orientation of about 45°. The convoluted and complex 10% surface, which should be similar to the outside boundary of the jet, is conical in shape and dominated as expected by small spatial scales. The conical and symmetric appearance of this external surface implies that the self-similar rescaling applied to our instantaneous data (even though self-similarity in this flow is based on mean quantities) is valid. Tendrils of ambient fluid are being drawn into the upstream end of the large-scale structure in the 30% surface (around the bottom quarter of the surface) at an angle of about 45° – an example of the large-scale entrainment mechanism described by Komori & Ueda (1985) and Dahm & Dimotakis (1987). Clumping of the jet fluid along the downstream dimension into an arrowhead-shaped structure, what we might expect to see for coherent structures in the axisymmetric mode, is evident in the 50% surface. These large-scale structures upon visual inspection appear to be of aspect ratio 2:1 (downstream to radial dimension) in this surface. This result agrees with our previous x-y-t autocorrelation results (Yoda *et al.* 1992), where we reported a 'spacing' between our large-scale structures of the order of two large-scale passage times for the 67% isoconcentration surface. In the highest-concentration surface (80%), two isolated pieces of high-concentration fluid are visible in the centre of our structure.

The spiral should be most evident at higher concentrations, because the lower-concentration fluid tends to be almost stationary fluid that has been expelled from the jet core. If we then look at an intermediate surface (50%) from four view angles spaced 45° apart (Figure 10), we see that the arrowhead-shaped structure is roughly axisymmetric, and it does not appear to be superimposed upon a spiral (i.e. like a set of beads strung on a spring). The bottom of this clumped structure is almost conical, and at about a 45° angle to the horizontal, due perhaps to the entrainment of ambient fluid there along this direction seen in the 10% surface. If we visualize the 50% isoconcentration surface for the second $Re = 4000$ natural jet case at the same four view angles (Figure 11), we see the downstream and upstream ends of two such clumped structures at the top and bottom, respectively, of the picture and nothing in the centre; note again that the downstream end of the upstream (upper) clump is again arrowhead-shaped. Although results are not presented here, we have looked at numerous isoconcentration surfaces at other thresholds for both $Re = 4000$ realizations and we have not seen indications of a spiral in any of them, despite the presence of numerous antisymmetric slices (upon visual inspection).

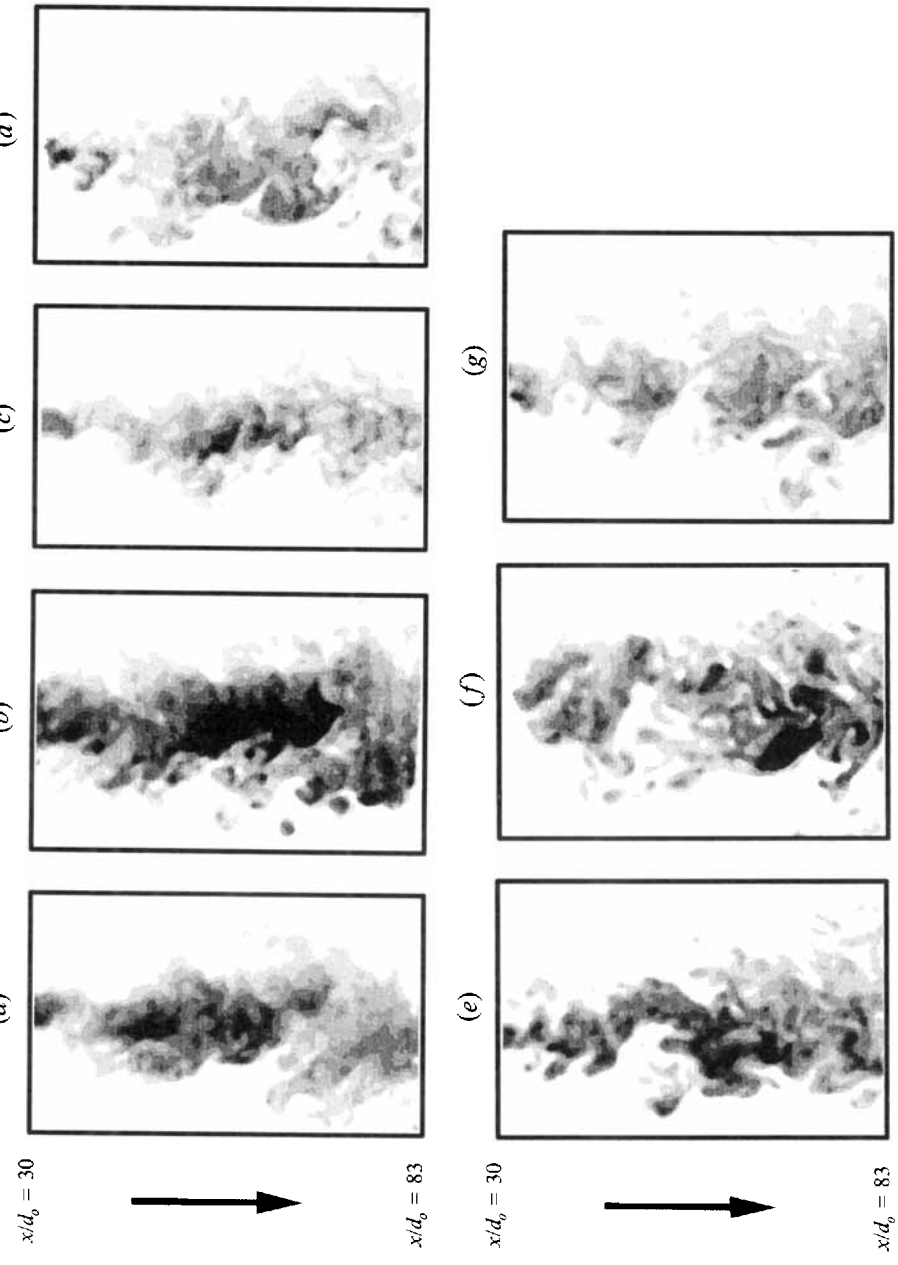

FIGURE 8. Rescaled axial slices for all seven cases: (*a*) $Re = 4000$ natural jet (case I); (*b*) $Re = 4000$ circularly excited jet; (*c*) $Re = 2000$ natural jet; (*d*) $Re = 2000$ circularly excited jet; (*e*) $Re = 1000$ natural jet; (*f*) $Re = 1000$ circularly excited jet; and (*g*) $Re = 1000$ buoyant jet. These slices, which correspond to the 0° centreline slice, are 240 rows by 150–180 columns. The number of distinct grey scales has been limited to 10 to enhance contrast. Note the strongly antisymmetric appearance of slices (*a*, *b*, *c*, *e* and *f*).

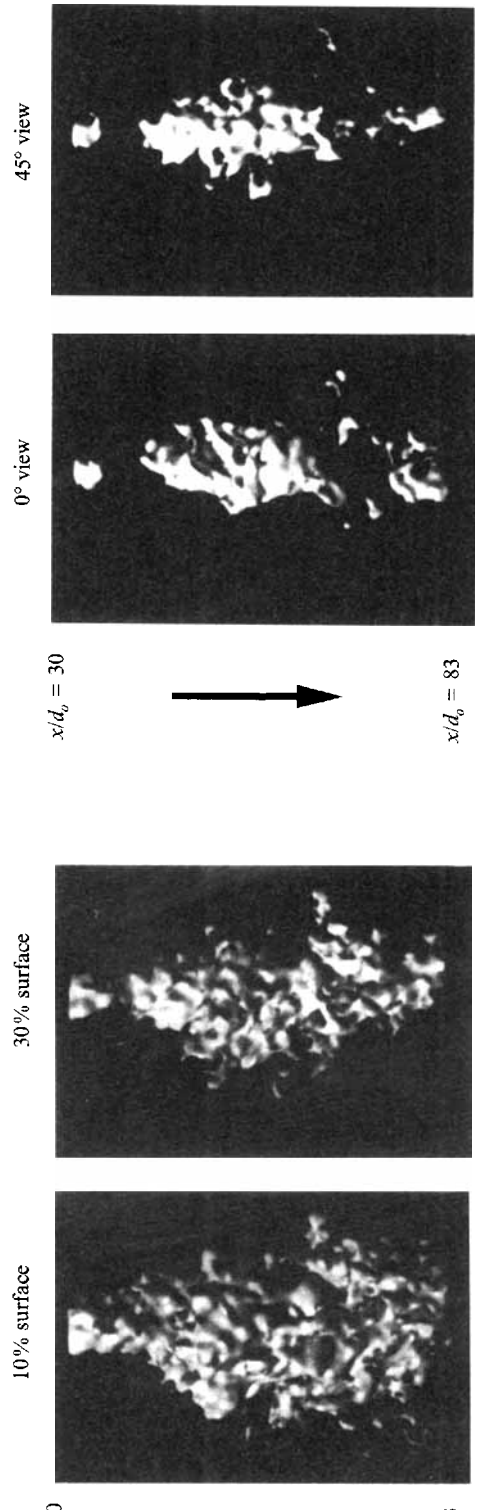

FIGURE 9. Different isoconcentration surfaces for the $Re = 4000$ natural jet (case I). The surfaces at 10, 30, 50 and 80% (of the maximum concentration value) are shown. In all cases, the viewpoint remains constant, at approximately 45° (cf. figure 7).

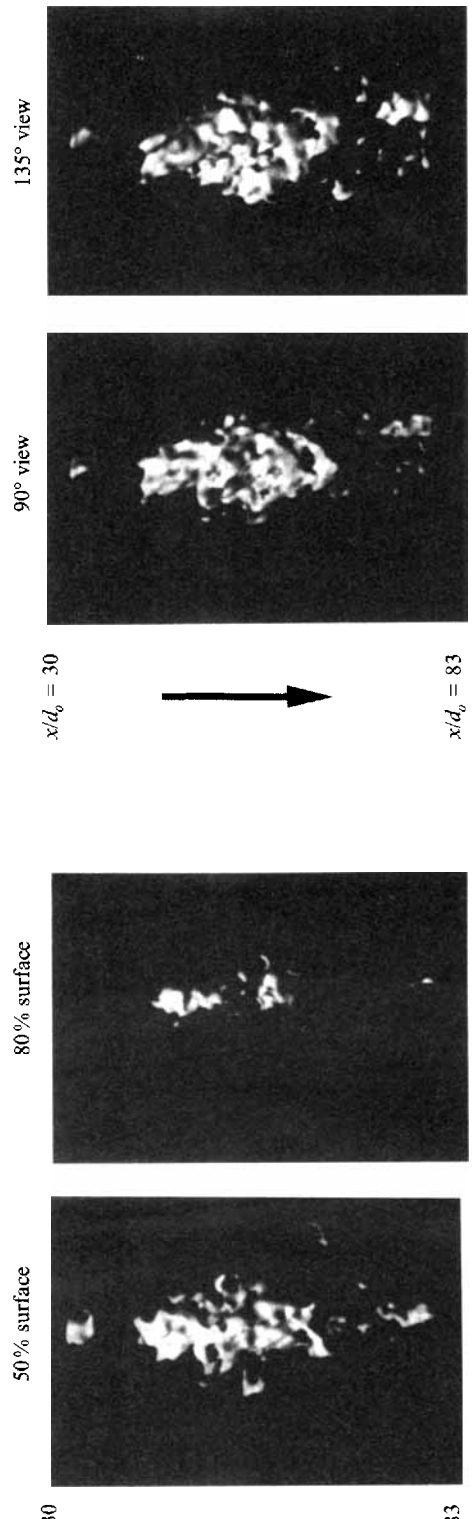

FIGURE 10. Different views of the 50% (of maximum) isoconcentration surface for the $Re = 4000$ natural jet (case I). Note the axisymmetry of the 'clump' in the centre.

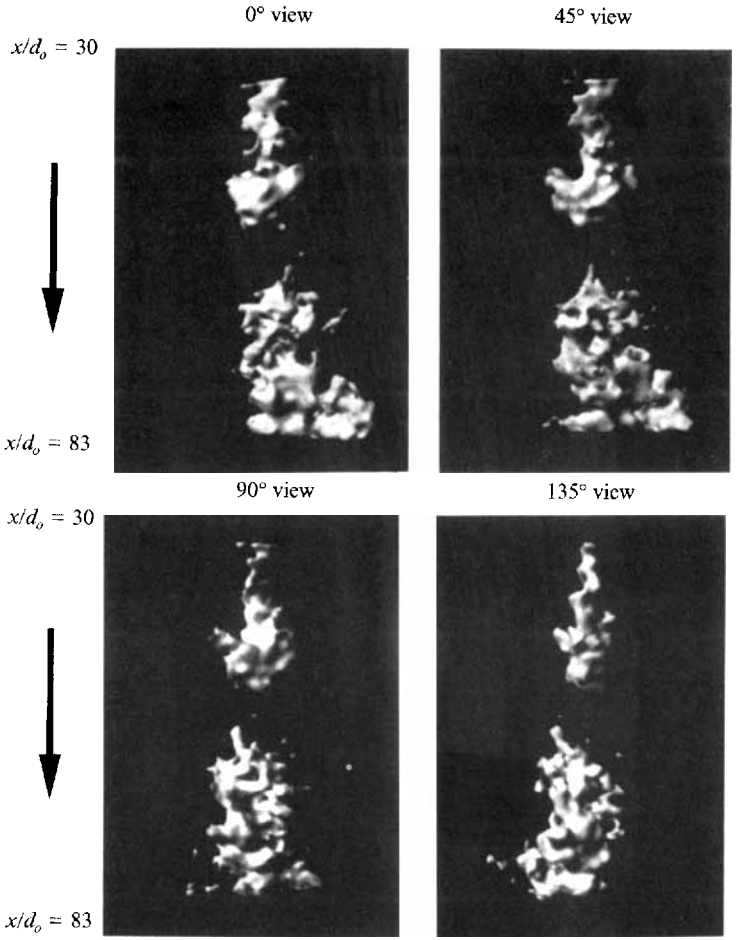

FIGURE 11. Same as figure 10, but for the second $Re = 4000$ natural jet case. Note the downstream and upstream ends of the two clumps at the top and bottom, respectively, of the picture.

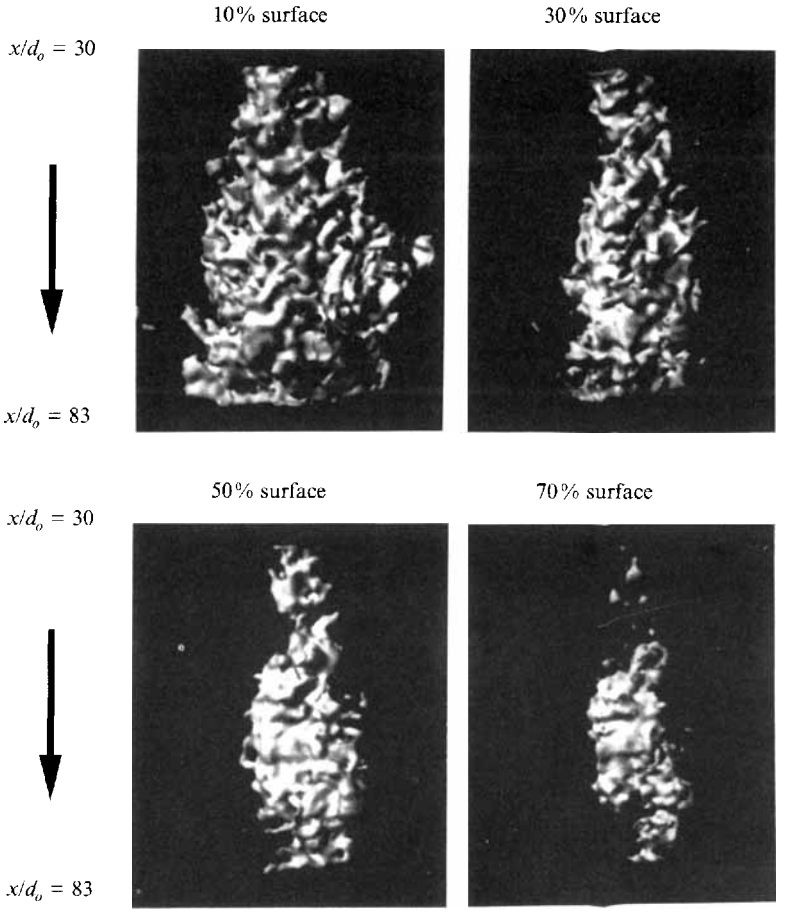

FIGURE 12. Different isoconcentration surfaces for the $Re = 4000$ circularly excited jet (St=0.3). Surfaces at 10, 30, 50 and 70% of the maximum concentration value are shown.

Figure 12 shows isoconcentration surfaces for a range of threshold concentrations for the circularly excited jet (10, 30, 50 and 70%). The view, about 45°, is identical to that used in figure 9. The 10% surface looks much more disorganized than its natural jet counterpart, and is dominated by small spatial scales of similar size. Not surprisingly, the clumping of the higher-concentration fluid along the downstream dimension that we saw in the natural jet is not as evident, even in the 50 and 70% surfaces, indicating that the circular excitation has suppressed this structure in the axisymmetric mode. The flow appears to be generally more disorganized owing to the large-amplitude circular excitation, and the higher threshold concentration surfaces imply that the centreline of this jet is much more distorted away from the vertical.

Although again our St_f is too large to excite resonant interactions with the helical mode, we would still expect to see some evidence of the helical mode if it is as dominant as theory predicts. To this end, four views rotated by 45° are depicted in figure 13. Again, no clear spirals (or persistent zigzags) are evident in any of these views. The 90° view of the 50% surface shows a clump with an arrowhead-shaped downstream end not unlike that in figures 10 and 11.

4.3. *Re = 2000: natural and circularly excited jets*

Figures 8(*c*) and 8(*d*) show rescaled centreline slices for both the natural and circularly excited jet. The natural jet axial slice has a clearly antisymmetric or zigzag outline, and we initially thought that this case represented our best chance to see the helical mode in a three-dimensional rendering. The circularly excited slice again shows the enhanced spreading rate due to nozzle excitation. The slices are narrower than their higher-*Re* counterparts, in part because the virtual origin is further downstream for this case.

Figure 14 depicts surfaces at different threshold concentrations for the natural jet at an angle of approximately 45°. The surfaces look generally less disorganized than the higher-*Re* case. A zigzag shape is clearly visible in the 15° view of the 30% surface (figure 15), but if this surface is viewed at various orientations, we see that although it appears to be antisymmetric with respect to the jet axis from one viewing angle, a perpendicular view from 105° results in a surface with a symmetric outline (the 15° viewing angle was chosen because the surface from this view showed the most clearly zigzag outline of all the views). The other two angles (60° and 150°) are then the intermediate views. So the zigzag shape seen in two-dimensional slices of the jet appears in three dimensions to actually be a simple sinusoid, instead of a spiral. The clumping of higher-concentration fluid seen in the higher-*Re* case is much less evident here.

Looking at the different isoconcentration surfaces at an orientation identical to that used in figure 14 for the corresponding circularly excited case (figure 16), we see again that circular excitation results in a much more disorganized flow, even in the far field. As in all the cases described in this section, we have inspected numerous isoconcentration surfaces not presented here for each dataset from various perspectives and failed to see any helical shapes.

4.4. *Re = 1000: natural, circularly excited and buoyant jets*

Figures 8(*e*), 8(*f*) and 8(*g*) show rescaled centreline slices for the natural, circularly excited and buoyant jet. In all cases except the buoyant jet, the intrusions of ambient fluid appear to be antisymmetric with respect to the jet centreline, giving the slices a zigzag appearance. If we look at isoconcentration surfaces at various thresholds for the natural, circularly excited and buoyant jet cases (figures 17–19), all again at

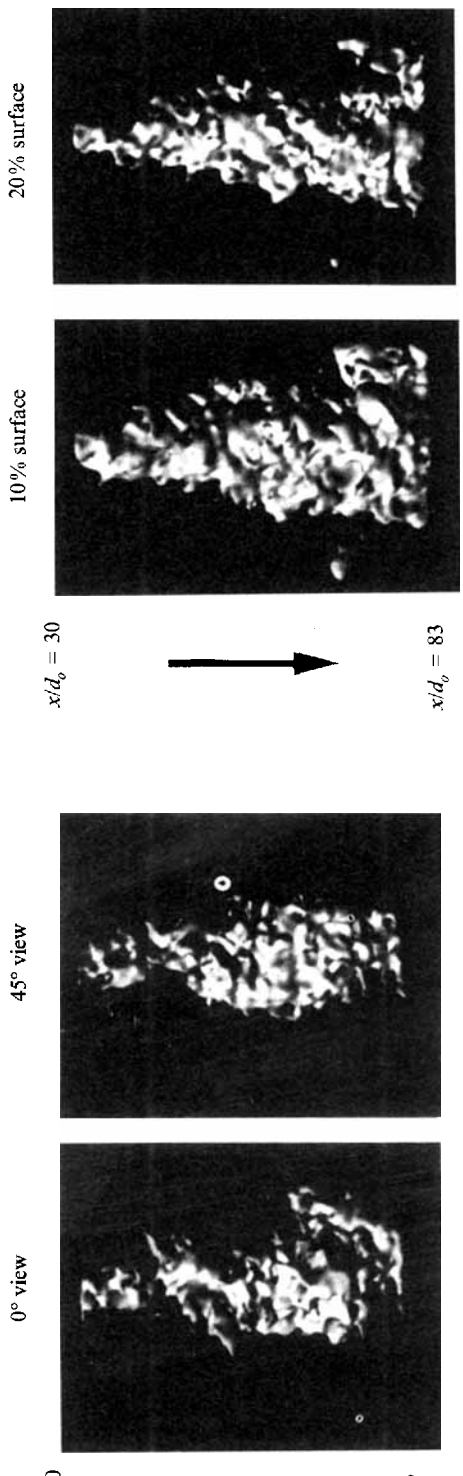

FIGURE 13. Different views of the 50% isoconcentration surface for the $Re = 4000$ circularly excited jet.

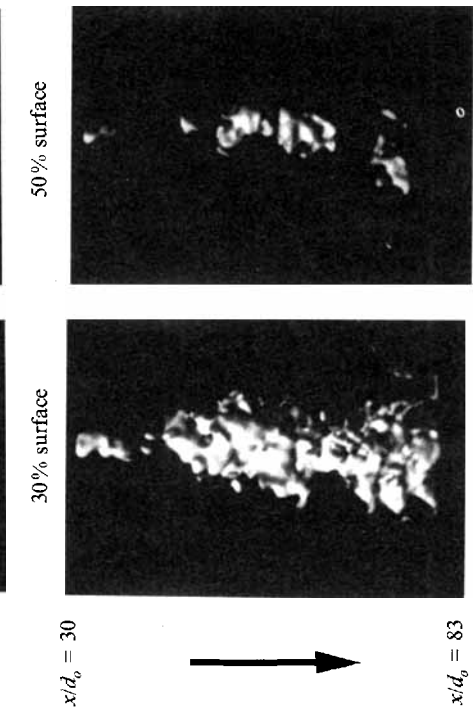

FIGURE 14. The 10, 20, 30 and 50% isoconcentration surfaces for the $Re = 2000$ natural jet. The surfaces are shown from the same viewpoint as in figure 9.

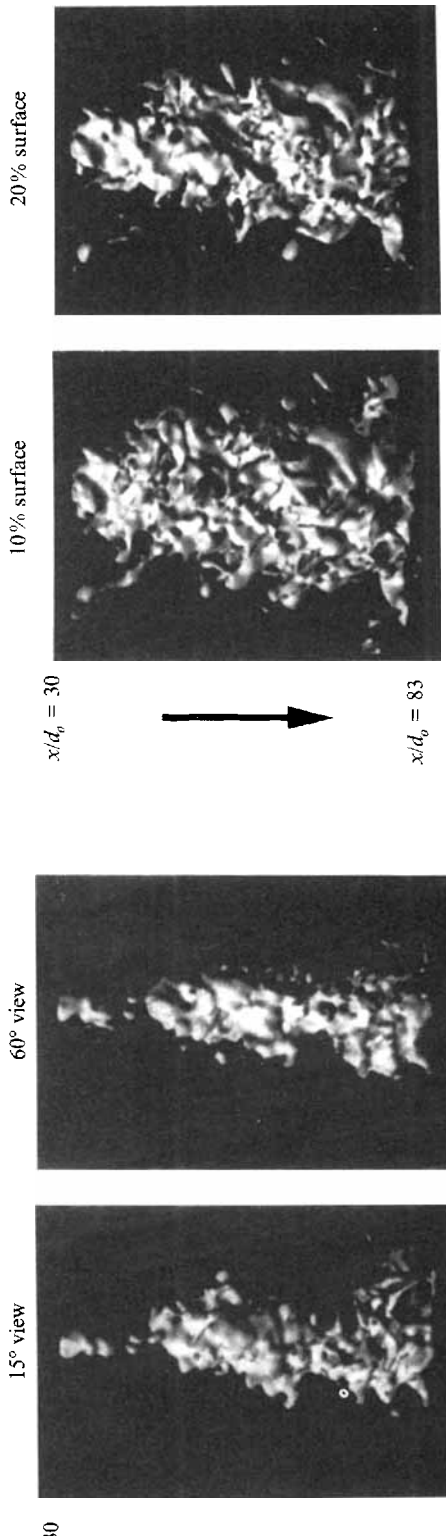

FIGURE 15. Similar to figure 10, but for the 30% surface of the $Re = 2000$ natural jet. Although the 15° view shows a clearly zigzag outline, the orthogonal 105° view is straight, implying that this surface is a sinusoidal column in three-dimensional, rather than the spiral corresponding to the helical instability mode.

FIGURE 16. Similar to figure 14, but for the circularly excited case (St=0.3).

an orientation angle of about 45°, we see no indication of a spiral in any of these surfaces. The highest-concentration surfaces for the natural and circularly excited jets (figures 17 and 18) show that the highest-concentration fluid is now evenly distributed in the downstream direction at this *Re*. The buoyant jet has a very uneven distribution of high-concentration fluid along the downstream direction (see for example the 70% surface in figure 19), consistent with the results of Papantoniou & List (1989), who reported that the concentration field of buoyant jets was 'very intermittent' and that local concentrations could reach values up to three or four times the mean level, compared to the two times reported for natural jets by Dahm & Dimotakis (1990). Again, the dominant spatial scale in all the Re=1000 surfaces appears to be larger than for the higher *Re* cases. The (slices of the) weakly buoyant case appears to be the most qualitatively similar to the pictures in Dimotakis *et al.* (1983) at $Re \leqslant 2300$, with its marked intrusions of ambient fluid and prominent hammerhead-shaped structures.

4.5. *Concentration field statistics*

Figure 20 shows the non-dimensionalized concentration centroid coordinates for all seven of the jet cases. In all cases, the coordinates have been smoothed by uniformly lowpassing over ten adjacent points. A spiral centroid (which would mean that a spiral shape existed in the concentration field, corresponding to the helical mode) would look like a spiral in our non-dimensionalized centroid coordinates; whether it spiralled in or out (or remained in a circular orbit) as x increases would depend on the pitch of the spiral. None of the centroids show a spiral shape, and some of the centroids (e.g. *a*, *c* and *f*) are roughly sinusoidal, waving back and forth as x increases. Not surprisingly, the circularly excited jet cases have the largest range of centroid variation.

Figure 21 shows the area inside several isoconcentration contours in a (y,z)-cross-section of the data as a function of downstream location x for both of the Re=4000 natural jet cases. The area has been normalized by the maximum value in the data, and also by $(x - x_o)^2$ to account for the (mean) spread of the jet. The curves for concentrations higher than 30% in the graph for case I have nearly zero area for x/d_o below 40 and above 65. This lack of higher-concentration fluid in the downstream dimension will result in the large-scale structure or arrowhead-shaped 'clump' clearly visible in the 50% surface in figure 9. If we assume that the downstream extent of this large-scale structure of $25d_o$ ($= 65d_o - 40d_o$) is independent of threshold concentration, this downstream extent is of the order of the local mean jet width at the midpoint downstream location of $x = 53d_o$.

Similarly, the higher-concentration curves in the case II plot clearly show almost no higher-concentration jet fluid present between x/d_o values of 50 and 60, corresponding to the region between the downstream and upstream ends of the two clumped structures visible in figure 11. Note that the area inside the circular isoconcentration contour expected in time average would be a horizontal line in these non-dimensionalized coordinates. The sharpest drop in area is between the 10 and 20% contours, owing to the large amount of almost stationary low-concentration fluid which the jet ejects and then eventually re-entrains. Figure 22 shows the area inside the 50% isoconcentration contour for the two Re=4000 natural jet cases and the $Re = 1000$ natural jet, as well as the area inside the 30% isoconcentration contour for the $Re = 2000$ natural jet (see the corresponding isoconcentration surfaces in figures 10, 11, 15, and 17) grouped again in terms of Reynolds number. In agreement with

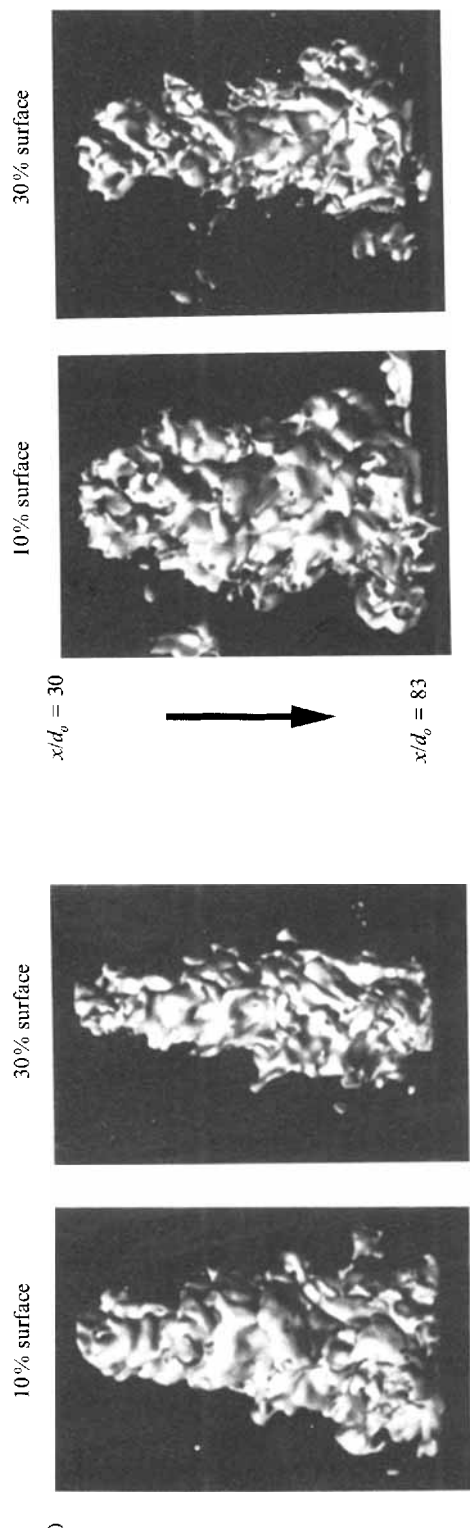

FIGURE 17. Different isoconcentration surfaces for the $Re = 1000$ natural jet. The 10, 30, 50 and 70% surfaces are presented here. The surfaces are shown from the viewpoint used in figure 9.

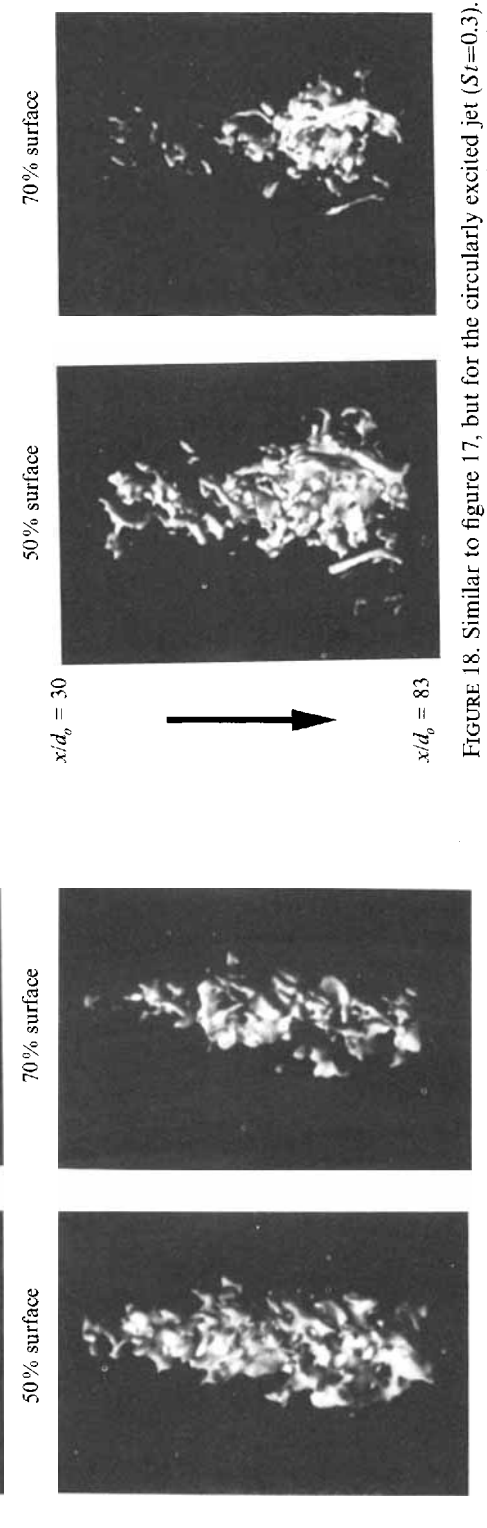

FIGURE 18. Similar to figure 17, but for the circularly excited jet (St=0.3). Note again the more disorganized appearance of the isoconcentration surfaces due to the circular excitation.

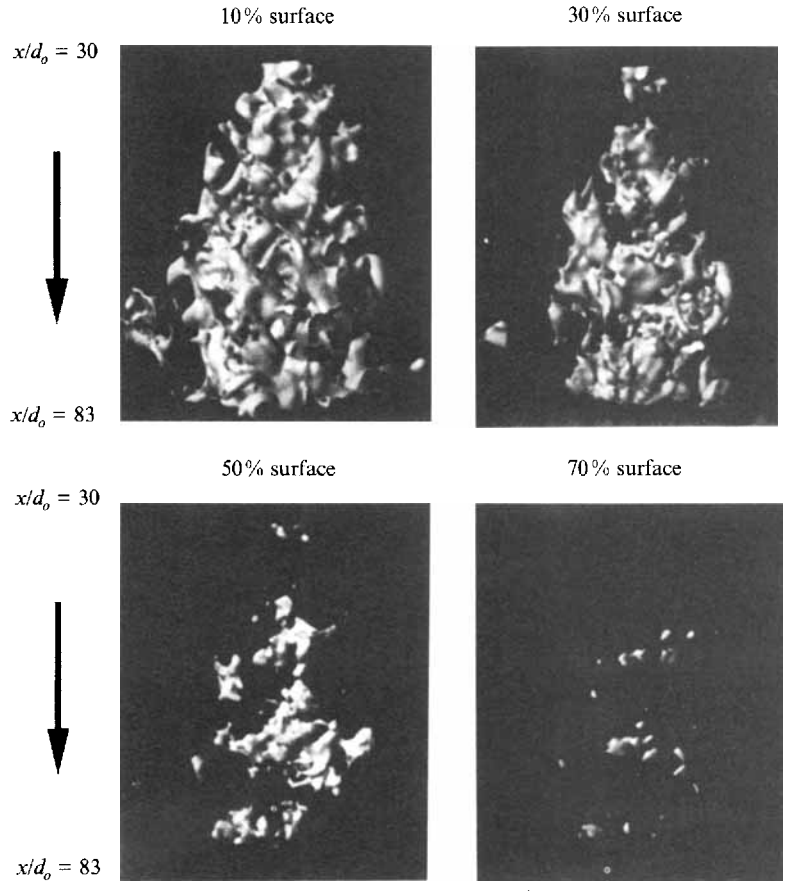

FIGURE 19. Similar to figure 17, but for the (weakly) buoyant jet. Note the large hammerhead-shaped structure on the lower right-hand side of the 10% surface, like those reported by Dimotakis *et al.* (1983).

the isoconcentration surface results, the clumping of the higher-concentration jet fluid is not visible at the two lower *Re*.

4.6. *Discussion of concentration results*

Large-scale organized structures are evident in the far field of the $Re = 4000$ jet in the form of roughly axisymmetric 'clumps' of higher-concentration fluid. These structures are approximately conical at the downstream edge due to entrainment of ambient fluid into the upstream end of the next structure downstream, and are in downstream extent of the order of the local jet width $\delta(x)$. This clumping is the three-dimensional analogue of the large regions of nearly constant-concentration fluid observed by Dahm & Dimotakis (1987) in planar concentration measurements in liquid jets and

FIGURE 20. Non-dimensionalized centroid coordinates $\zeta(x)$ *vs.* $\xi(x)$ for: (*a*) the $Re = 4000$ natural jet (case I); (*b*) the $Re = 4000$ circularly excited jet; (*c*) the $Re = 2000$ natural jet; (*d*) the $Re = 2000$ circularly excited jet; (*e*) the $Re = 1000$ natural jet; (*f*) the $Re = 1000$ circularly excited jet; and (*g*) the $Re = 1000$ buoyant jet. The square indicates the furthest upstream location for each case, and the arrows indicate the flow direction. The plusses mark centroid coordinates evenly spaced about $9d_o$ apart along x. The ζ- and ξ-axes have identical dimensions.

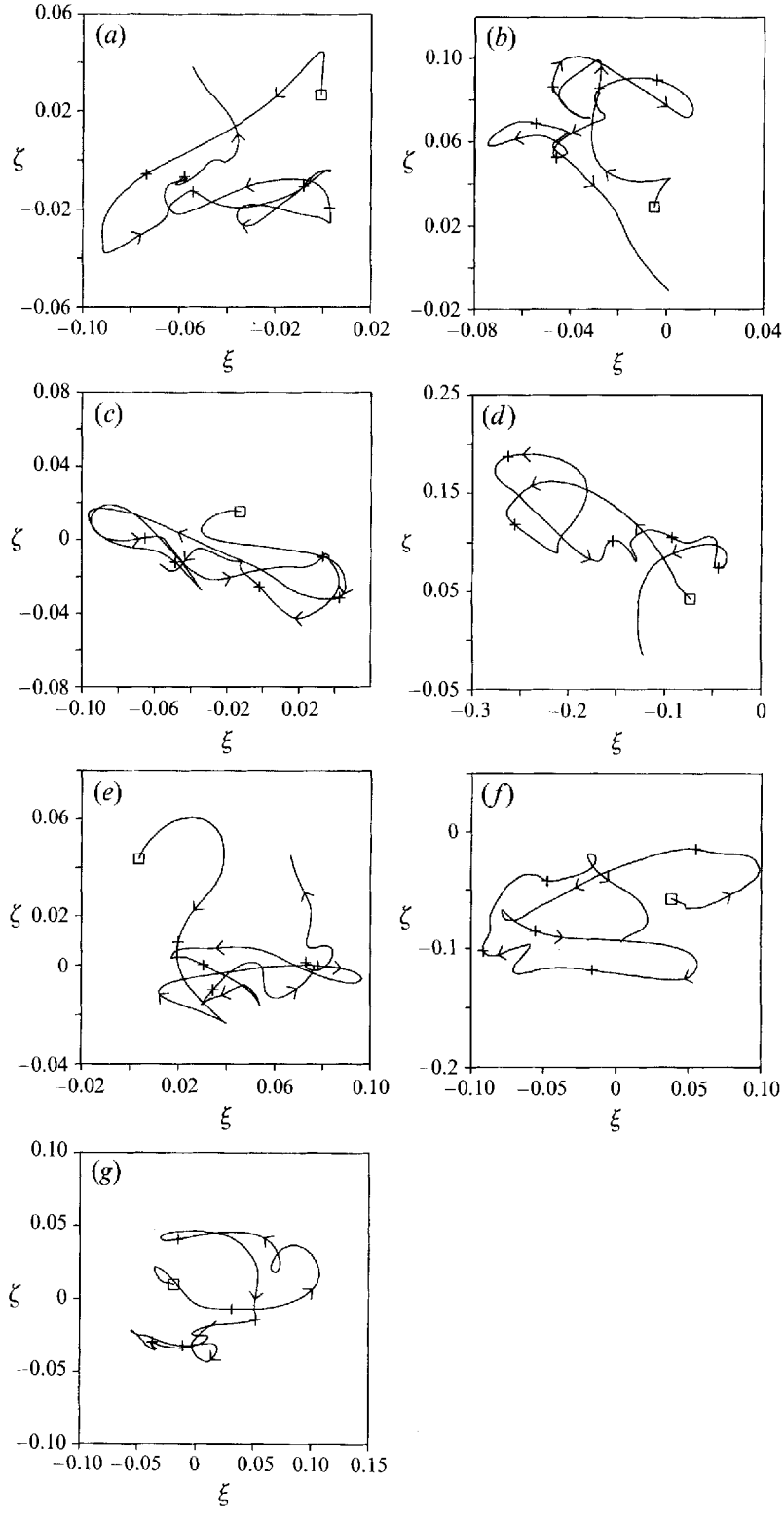

FIGURE 20 (*a–g*). For caption see facing page.

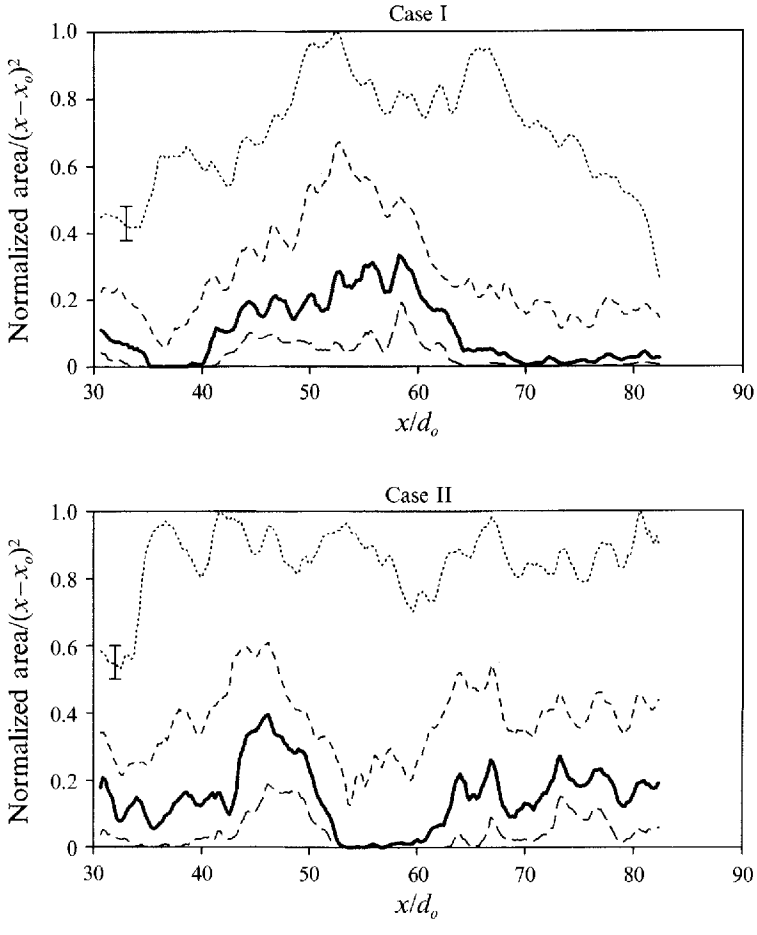

FIGURE 21. Normalized area inside a isoconcentration contour in a $y-z$ slice of the data as a function of x/d_o for both cases of the $Re = 4000$ natural jet: case I and case II. The maximum area has been rescaled to unity. Data are shown for the 10, 30, 50, and 70% of maximum concentration contours (labelled in the case II plot; the case I graph uses identical line types). The area inside the 50% contour is depicted with the thick line. All data have been normalized by the maximum area as well as by $(x-x_o)^2$ to account for the spread rate. An error bar is shown on the left side for the 10% curve (based on the $\pm 5\%$ r.m.s. error).

the 'ramps' spaced at about a single large-scale passage time observed in single-point concentration measurements by Dowling & Dimotakis (1990) in gaseous jets. These structures are present in our data at only the highest Re; this result, when considered with the 'flame length' results of Dahm & Dimotakis (1987), suggests that this large-scale structure is unique to fully turbulent jets.

Although organized large-scale structure is evident in this flow, we have failed to see any evidence of the helical mode predicted by stability theory. It is possible that the number of realizations analysed here is too small to capture the expanding spiral structure hypothesized by Dimotakis *et al.* (1983), but experimental and theoretical evidence suggest that this structure should be both robust and common. Mungal, Lozano & van Cruyningen (1992) reported from temporal and axial visualizations of a $Re = 2 \times 10^8$ air jet that organized large-scale structure in the far field of this flow was clearly evident, present at almost all downstream locations (robust) and most

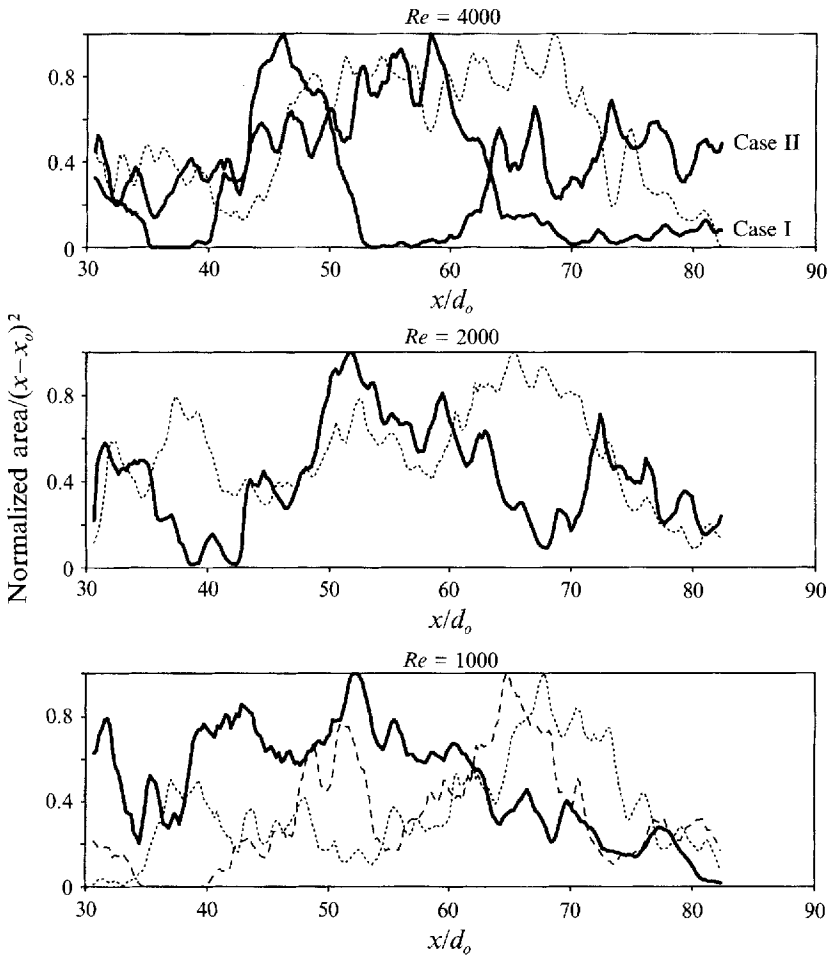

FIGURE 22. Similar to figure 21, but only for the area inside the 50% contour for the Re=4000 and 1000 jets and the 30% contour for Re=2000 jets. In all the plots, the natural jet case is the heavy solid line (both cases I and II are shown as marked in the Re = 4000 plot), the circularly excited case is the dotted line and the buoyant case is shown by the dashed line. Again, the maximum area has been rescaled to unity.

importantly, present at almost all times in the flow (common). Similar experiments in the self-similar region of a water jet of Re = 5000 (Yoda *et al.* 1992; carried out in the same facility as the present results) verified these results, and in addition implied that circular forcing at St = 0.3 enhanced the presence of antisymmetric structures, and therefore the helical mode.

Based on the robustness and presence of this large-scale structure in the flow at almost all times, we thought that our chances of seeing the helical mode in an instantaneous three-dimensional visualization over a large extent of the jet as a spiral were excellent. The three-dimensional data from both natural (unforced) and circularly excited jets show, however, that the far field of the jet in three dimensions is not in the form of an expanding spiral, but instead appears to be in the form of a simple sinusoid, even when two-dimensional slices of the data are clearly antisymmetric in shape. In other words, the antisymmetric patterns seen in axial slices of the jet far field appear to be parallel slices of a simple sinusoid in three

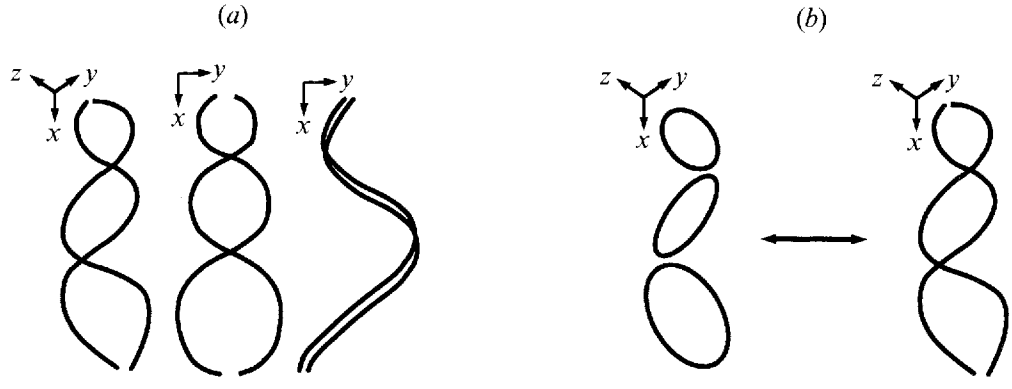

FIGURE 23. (*a*) Cartoon of the ± 1 helices. These paired helices have a symmetric outline from the view along the z-axis (x-y projection) and an antisymmetric zigzag outline from the orthogonal view along the y-axis (x-z projection). x is the flow direction. (*b*) The spiral vortex filaments pictured in (*a*) could originate via vortex reconnection interactions from the near-field column of tilted vortex loops.

dimensions, instead of radial slices of an axisymmetric spiral. This result is quite unexpected.

We propose based on these results that the structure of the far field of the jet consists not of a single expanding spiral, but of a pair of expanding counter-rotating helical vortex filaments, or ± 1 helices (B. J. Cantwell 1992, private communication) (figure 23*a*). This model is based upon the following four factors:

(*a*) The ± 1 helices are in agreement with theory, which predicts that the $n = +1$ and $n = -1$ modes are equally unstable (and therefore equally common). Furthermore, the coexistence of these counter-rotating helices gives a swirl-free flow.

(*b*) In terms of large-scale structure, ± 1 helices would result in the axisymmetric clumping of higher-concentration fluid seen in our and other researchers' results.

(*c*) This structure could explain two-dimensional experimental results (e.g. Mattingly & Chang 1974; the 'mode contamination' reported by Petersen *et al.* 1988; Yoda *et al.* 1992) which report the presence of both symmetric and antisymmetric structures in two-dimensional measurements in the near and far fields. Both the axisymmetric ($n = 0$) and the 'multiple' helical ($|n| \geqslant 2$) modes lead to shapes which are always symmetric about the jet axis. Therefore only the combination of the $n = \pm 1$ modes will result in a structure with both symmetric and antisymmetric axial slices, depending upon the azimuthal orientation. If these counter-rotating spirals rotate about their (the jet) axis, we would expect to see both antisymmetric and symmetric patterns in even a stationary two-dimensional axial visualization.

(*d*) In terms of the origins of this far-field structure, it seems plausible that this counter-rotating pair of helices could be caused by vortex reconnection interactions (Schatzle 1987; Kida, Takaoka & Hussain 1991) between the tilted near-field vortex rings (Hussain & Zaman 1981; Parekh, Leonard & Reynolds 1988) as they are convected downstream and approach each other. Although the jet must remain swirl-free, fixing the relative amplitude of the two helices, their relative phase is most likely to be determined by the initial interactions between neighbouring tilted vortex rings (figure 23*b*). The vortex simulations of Martin (1991) of a near-field jet under $n = \pm 1$ excitation show a similar large-scale paired helix structure, and the reorganization of the two helical structures into a column of tilted and distorted ring-like structures.

We would expect from this model that the jet would be highly receptive, even in the far field, to a combination of axial and circular excitation. This proposed structure may therefore explain the bifurcating and blooming jet results of Lee & Reynolds (1985) and Parekh *et al.* (1988), who were able to drastically change the jet structure, even in terms of its far-field asymptotic state, with combined axial and orbital excitation at the jet nozzle.

Finally, this model unifies two instantaneous concentration fields proposed for the far-field modes of the jet based upon two-dimensional axial observations. The first model, proposed by Dahm & Dimotakis (1990) for the axisymmetric mode, consists of large symmetric regions of constant-concentration fluid. They showed that the resultant instantaneous stepwise downstream concentration decay converged over time to the smooth $1/x$ mean decay. Mungal & O'Neil (1989) proposed an analogous picture for the helical mode, consisting of *antisymmetric* or zigzag regions of constant concentration, again associated with an instantaneous stepwise concentration decay, and hypothesized that the jet continuously 'switches' between the axisymmetric and helical modes. The entrainment predicted by these two models, which is visible in the work of Shlien (1987), coexist in the paired helix model – they are simply two-dimensional 'slices' of the same structure at different orientations.

The data presented and analysed here have deliberately been biased towards the axial slices which showed the most antisymmetric patterns. This criterion was based on simple geometric arguments – a two-dimensional slice of a spiral along its axis is a zigzag – and previous axial visualizations, which equated antisymmetric or zigzag shapes in the far field of the jet with the presence of the helical mode. Although it is possible that we are investigating atypical data, we have clearly shown that the far field of the jet is not in the form of an expanding spiral, even when two-dimensional slices of the jet are antisymmetric, since it is geometrically impossible for a slice of such a shape to be symmetric with respect to the jet axis. In addition, if the jet is in the form of a (rotating) double helix, the data here actually are representative – and only the orientation between the image planes and the paired helices has been biased.

Our proposal that the jet is in the form of a double (rather than single) helix is certainly not the only possible explanation for the results, but it is suggested as the simplest model which appears to fit both experiment and theory. Note that of the modes predicted by linearized stability theory, only the combination of the $n = \pm 1$ modes would give rise to a structure which is symmetric from one viewpoint and antisymmetric from the orthogonal viewpoint. In addition, the model provides a logical explanation of how the proposed far-field structure originates from the commonly accepted near-field structure.

4.7. *The concentration gradient*

In addition to deducing the large-scale structure and modes of the self-similar region of the jet, we can use our concentration data to investigate and characterize the structure of this flow at intermediate ($\approx O(\lambda_K)$) spatial scales. We expect that our picture at these scales will be typical of turbulent free shear flows.

Before analysing the local topology of every point in the flow, critical-point distributions were obtained for extensively smoothed concentration gradient fields of the three $Re = 1000$ cases (Yoda 1992). Since smoothing represses the smaller-scale structure and noise, the results pertain only to the concentration field at coarse spatial scales ($> \lambda_K$); the data were lowpass filtered over a $3 \times 3 \times 3$ window four times, resulting in a spatial resolution nine times more coarse than that used for the iso-concentration surfaces. The results from these coarsely sampled concentration fields

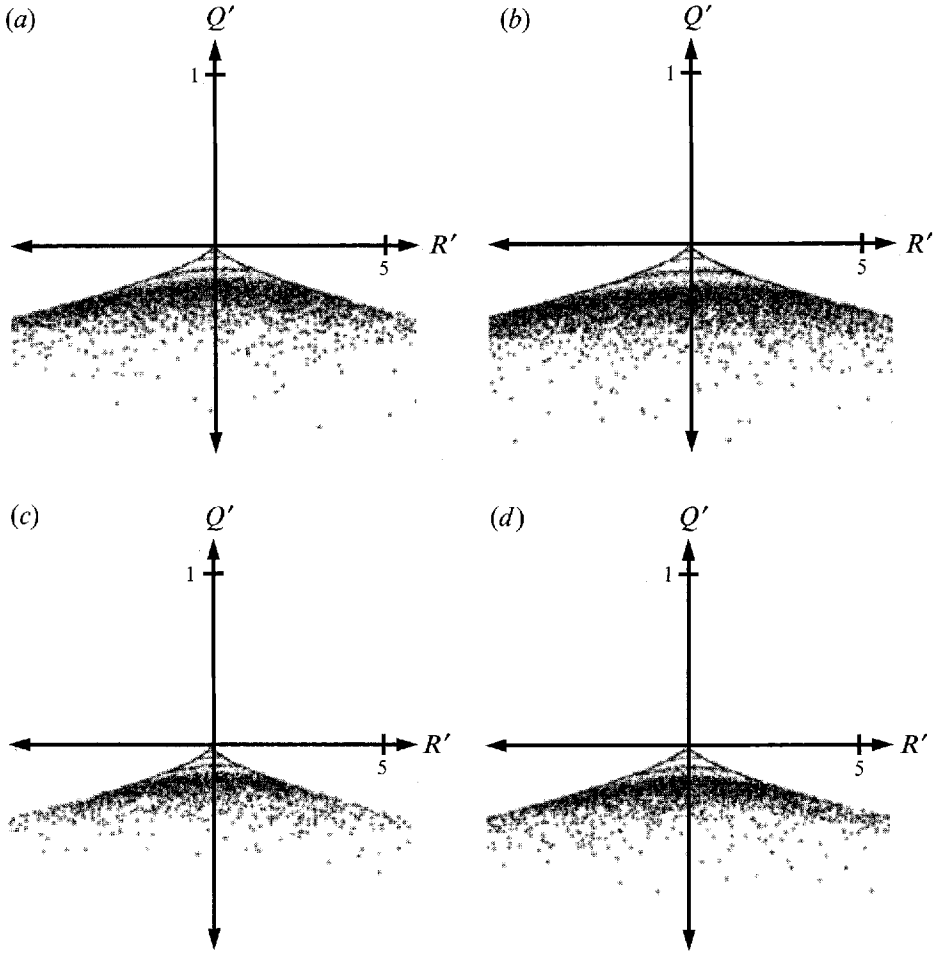

FIGURE 24 (*a–d*). For caption see facing page.

imply that the the buoyant jet concentration field has the greatest number of repelling nodes (i.e. isolated local minima), followed by the circularly excited and then natural jet fields, with the number of repelling nodes for the buoyant and circularly excited cases exceeding that for the natural jet by 50–100%. Physically, this implies that on an intermediate scale more isolated 'pockets' of lower-concentration or ambient fluid are present in the interior of the buoyant jet than in that of either the circularly excited or natural jet. Despite the limited sample space and spatial resolution, this result is consistent with the buoyant jet results of Papantoniou & List (1989), who reported that 'the ambient fluid presence in the flow interior is greatly increased' in the presence of buoyancy.

We now extend these critical-point classification methods to every point in the jet flow. Figure 24 shows our transformed trace-free data plotted in the (Q', R')-plane $(P' \equiv 0)$ for all seven cases. These modified scatter plots are all qualitatively similar, with the bulk of the datapoints near the cusp of the S_1' curve. The contour for 1000 points is closest to the origin (i.e. has the largest Q'), followed by the 100 and 10 point contours, respectively. In addition, the points appear to be evenly distributed between the right $(R' > 0)$ and left $(R' < 0)$ half-planes. The most striking feature of these

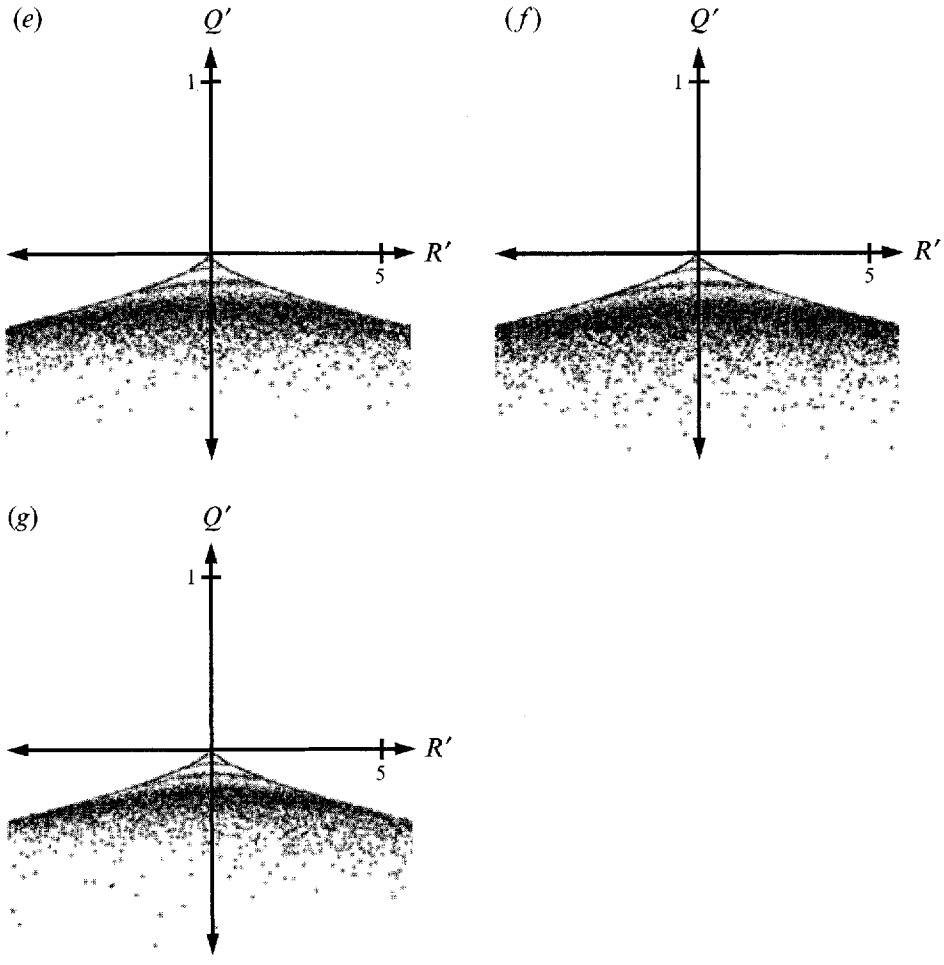

FIGURE 24. $Q' - R'$ plots for the seven flow cases: (*a*) Re=4000 natural jet (case I); (*b*) Re=4000 circularly excited jet; (*c*) Re=2000 natural jet; (*d*) Re=2000 circularly excited jet; (*e*) Re=1000 natural jet; (*f*) Re=1000 circularly excited jet; and (*g*) Re=1000 buoyant jet. Contours are drawn through points where 1, 10, 100 and 1000 points overlap; note that a 'contour' through a single point is identical to a simple scatter plot. The contours through 10, 100 and 1000 points are progressively closer to the origin. Each plot comprises between 80 000 and 180 000 points. The axes have arbitrary units, and are identical in dimension for all seven cases. Note that the R'-axis spans a range five times that of the Q'-axis.

plots, which describe the local topology of the concentration gradient field, however, is that outside of the cusp region, the data tend to 'hug' the curve S_1', implying that these points locally have a nearly axisymmetric topology (saddle-saddle-star nodes, in the terminology of Chong *et al.* 1990). Virtually none of the data lie in the region of two-dimensional topologies, or near the negative Q'-axis away from the origin.

The (Q', R')-scatter plots of the data with white or zero mean noise were qualitatively similar to those for the original data (Yoda 1992), but those for the data with (severe) biased noise were *asymmetric*, with far more points in the $R' > 0$ half-plane. Figure 25 shows such a plot for the $Re = 1000$ natural jet case with biased (+20% maximum) noise; the data are clearly biased towards the right half-plane in comparison with the (Q', R')-plot for the original data (Figure 24*g*).

Large magnitudes of R' are associated with large magnitudes of the concentration

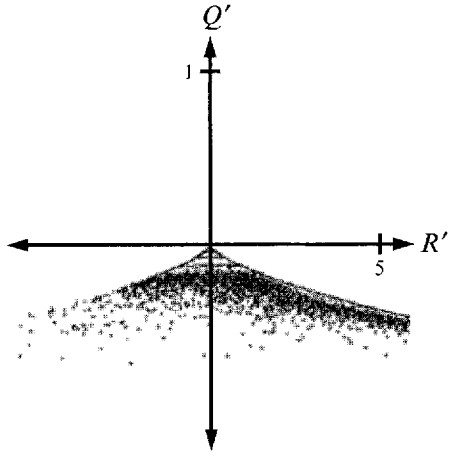

FIGURE 25. Q'-R' scatter plot for the $Re = 1000$ natural jet data with 'biased' noise. Randomly generated values of up to 20% of the maximum concentration value were added to the original median filtered data; the resultant data were processed using methods identical to those used with the original data to obtain the concentration gradient and corresponding (Q', R') values. Note the pronounced asymmetry of the data.

gradient, since R' is proportional to the determinant of the Jacobian of ∇c. This implies that the concentration field in regions of the flow where $|\nabla c|$ is large (at least to this spatial resolution) tends to be axisymmetric, and is compressed along the axis of symmetry. Such a topology may correspond to a sheet (the nearly axisymmetric topology implies a sheet-like, rather than ribbon-like, structure) of fluid which is of significantly higher ($R' > 0$) or lower ($R' < 0$) concentrations than the mean value. Both types of sheets, which from the symmetry of the (Q', R')-plots about the Q'-axis are about equally common, would be associated with large values of $|\nabla c|$.

Ruetsch & Maxey (1991) have reported in DNS studies of low-Prandtl-number ($Pr \leqslant 1$) homogeneous turbulence that the largest passive scalar dissipation values ($25 - 30\overline{|\nabla T|^2}$) are associated with sheet-like structures of 10–20 times their thickness in planar extent. From their fully resolved concentration measurements in high-Sc flows, Buch & Dahm (1991) have reported that the scalar dissipation, and therefore $|\nabla c|$, field is composed almost entirely of thin, locally planar layer-like structures, with a thickness of $O(\lambda_B)$. Adjacent layer-like structures tended to remain locally parallel for 'many' layer thicknesses. Although these individual sheet-like structures cannot be seen in our lower spatial resolution measurements, the sheets implied by the (Q', R')-plots may be due to the superposition of several such adjacent locally parallel layers. So even at our resolution of 100 times the diffusion-limited spatial scale, regions of the passive scalar field with large values of $|\nabla c|$ appear to be organized into locally planar sheet-like structures.

5. Conclusions

We report here measurements of the virtually instantaneous three-dimensional concentration field in a round high-Sc jet of Reynolds number $Re = 1000$-4000 over the downstream distance range $30 \leqslant x/d_o \leqslant 83$. Circular excitation at a Strouhal number $St = 0.3$ was used to try to enhance the presence of the supposedly dominant helical mode. To our knowledge, these measurements are the first of this type.

To summarize, we go back to the issues raised in the Introduction. What is the instantaneous three-dimensional large-scale structure in the far field of the jet? Organized large-scale structure appears to exist in the far field of the fully turbulent ($Re = 4000$) jet in the form of roughly axisymmetric 'clumps' of higher-concentration (>50% maximum) jet fluid with a conical downstream end. These structures are about the local jet diameter in downstream extent, in agreement with results in both water and air jets (Dahm & Dimotakis 1990; Dowling & Dimotakis 1990).

How does the dominant helical mode predicted by stability theory 'shape' this large-scale structure? From previous work we expected to see the helical mode as a spiral in the three-dimensional concentration field, but we have not seen any such structures in our data. No spiral structures were evident even in the circularly excited cases. The antisymmetric two-dimensional axial images that we and other researchers had previously thought to be slices of a three-dimensional spiral appear to be slices of a simple sinusoid in three dimensions.

Our results suggest a revised picture of the large-scale structure in the self-similar region of the jet. Instead of a single spiral, as suggested by Dimotakis *et al.* (1983), the jet appears in the far field to consist of a pair of counter-rotating spirals, or ± 1 helices. This model has four advantages: (i) linear stability theory predicts that positive and negative (± 1) helices are equally dominant, and the ± 1 helices result in a swirl-free flow; (ii) this pair of helices would result in the large-scale structure observed in several flow visualization studies; (iii) this structure is consistent with previous experimental results; and (iv) this structure is a logical consequence of the jet near-field structure. As the near-field column of tilted and strained vortex rings approach each other, they should interact via vortex reconnection interactions to form this 'double helix' structure. The phase between the paired helices would then be determined by the initial near-field vortex ring interactions. This model unifies the two instantaneous concentration fields proposed for the axisymmetric and helical modes by Dahm & Dimotakis (1990) and Mungal & O'Neil (1989), respectively – both models are simply 'slices' of the same structure at different orientations.

Although circular excitation failed to enhance the presence of the helical mode (and should not, if the above model is correct), it did have two effects on the flow: (i) from the centroid results, it clearly distorts the jet centreline away from the vertical; and (ii) it appears to result in a qualitatively more chaotic-looking (smaller spatial scales) concentration distribution. Both effects are visible even in the far field of the jet. The weakly buoyant case ($Fr \approx 100$) appears to be the most qualitatively similar to the lower-Re cases visualized by Dimotakis *et al.* (1983).

Finally, what is the local structure of the concentration field? Even at this intermediate spatial resolution, regions with a large concentration gradient magnitude appear to be organized into locally planar sheet-like structures, with concentration values both significantly below and above the local mean. Our resolution is of course insufficient to resolve the fine-scale layers associated with large values of scalar dissipation (Ruetsch & Maxey 1991; Buch & Dahm 1991), but the sheets implied by our data may reflect the superposition of several of the locally parallel and adjacent fine-scale layers reported by Buch & Dahm at high Sc.

Our results suffer through two factors: (i) we are restricted by the limitations of current technology to measurement and analysis of a single or at best a few realizations of the flow; and (ii) in order to capture a few local flow widths, the spatial resolution of the measurements is two orders of magnitude above the diffusion-limited spatial scale. Nevertheless, even a single instantaneous three-dimensional realization at this spatial resolution of the passive scalar concentration in this turbulent high-Sc free shear flow

represents an advance in our measurement capabilities. Our data have enabled us to visualize in three dimensions the large-scale structure in a turbulent high-Schmidt-number flow. The antisymmetric shapes in two-dimensional axial images of the jet are not slices of a three-dimensional spiral, and appear instead to be slices of a simple sinusoid in three dimensions, suggesting that both the +1 and −1 helical modes are simultaneously present in the flow.

We wish to thank Professor Brian Cantwell, who suggested the critical-point analyses presented here, and who was invaluable in interpreting the physical significance of many of our results. We also thank Paul Ning for the use of his marching cubes software; Rolf Sondergaard and Wei-ping Cheng for the use of their topological analysis software, and Professor William Reynolds and Scott Smith for the development of the jet nozzle forcing apparatus. This work was funded by National Science Foundation grants ECS–8815815 and DDM–8914232. We are grateful for their support.

REFERENCES

ADRIAN, R. J. 1980 Multi-point optical measurements of simultaneous vectors in unsteady flow—a review. *Intl J. Heat Fluid Flow* **7**, 127–145.

BATCHELOR, G. K. & GILL, A. E. 1962 Analysis of the stability of axisymmetric jets. *J. Fluid Mech.* **14**, 529–551.

BECKER, A. & YAMAZAKI, S. 1978 Entrainment, momentum flux and temperature in vertical free turbulent diffusion flames. *Combust. Flame* **33**, 123–149.

BRADSHAW, P., FERRISS, D. H. & JOHNSON, R. F. 1964 Turbulence in the noise-producing region of a circular jet. *J. Fluid Mech.* **19**, 591–624.

BREIDENTHAL, R. 1981 Structure in turbulent mixing layers and wakes using a chemical reaction. *J. Fluid Mech.* **109**, 1–23.

BROADWELL, J. E. 1989 A model for reactions in turbulent jets—effects of Reynolds, Schmidt and Dahmköhler numbers. In *Turbulent Reactive Flows* (ed. R. Borghi & S. N. B. Murthy), pp. 257–277. Springer-Verlag.

BROWN, G. L. & ROSHKO, A. 1974 On density effects and large structure in turbulent mixing layers. *J. Fluid Mech.* **64**, 775–816.

BUCH, K. A. & DAHM, W. J. A. 1991 Fine scale structure of conserved scalar mixing in turbulent shear flows: Sc $\gg$ 1, Sc $\approx$ 1 and implications for reacting flows. *Rep.* 026779-5, The University of Michigan.

CANTWELL, B. J. 1981 Organized motion in turbulent flow. *Ann. Rev. Fluid Mech.* **13**, 457–515.

CHEN, C. J. & RODI, W. 1980 *Vertical Turbulent Buoyant Jets—A Review of Experimental Data.* Pergamon Press.

CHONG, M. S., PERRY, A. E. & CANTWELL, B. J. 1990 A general classification of three-dimensional flow fields. *Phys. Fluids* A **2**, 765–777.

CROW, S. C. & CHAMPAGNE, F. H. 1971 Orderly structure in jet turbulence. *J. Fluid Mech.* **48**, 547–591.

CRUYNINGEN, I. VAN 1990 Quantitative imaging of turbulent gaseous jets using planar laser-induced fluorescence. *HTGL Rep.* T-267, Mechanical Engineering Department, Stanford University.

DAHM, W. J. A. & DIMOTAKIS, P. E. 1987 Measurements of entrainment and mixing in turbulent jets. *AIAA J.* **25**, 1216–1223.

DAHM, W. J. A. & DIMOTAKIS, P. E. 1990 Mixing at large Schmidt number in the self-similar far field of turbulent jets. *J. Fluid Mech.* **217**, 299–330.

DAHM, W. J. A., DIMOTAKIS, P. E. & BROADWELL, J. E. 1984 Non-premixed turbulent jet flames. *AIAA Paper* 84–0369.

DAHM, W. J. A., SOUTHERLAND, K. B. & BUCH, K. A. 1991 Direct, high-resolution, four-dimensional measurements of the fine scale structure of Sc $\gg$ 1 molecular mixing in turbulent flows. *Phys. Fluids* A **3**, 1115–1127.

DIMOTAKIS, P. E., MIAKE-LYE, R. C. & PAPANTONIOU, D. A. 1983 Structure and dynamics of round turbulent jets. *Phys. Fluids* **26**, 3185–3192.

DOWLING, D. R. 1988 Mixing in gas phase turbulent jets. PhD thesis, California Institute of Technology.

DOWLING, D. R. & DIMOTAKIS, P. E. 1990 Similarity of the concentration field of gas-phase turbulent jets. *J. Fluid Mech.* **218**, 109–141.

EASTMAN KODAK COMPANY 1991 *Kodak Ektar 25 professional film.* Publication no. E–135.

FIEDLER, H. E. 1974 Transport of heat across a plane turbulent mixing layer. *Adv. Geophys.* **18A**, 93–109.

FIEDLER, H. E. 1988 Coherent structures in turbulent flows. *Prog. Aerospace Sci.* **25**, 231–270.

GOODMAN, J. W. 1968 *Introduction to Fourier Optics.* McGraw-Hill.

HUSSAIN, A. K. M. F. & ZAMAN, K. B. M. Q. 1981 The 'preferred mode' of the axisymmetric jet. *J. Fluid Mech.* **110**, 39–71.

KIDA, S., TAKAOKA, M. & HUSSAIN, F. 1991 Collision of two vortex rings. *J. Fluid Mech.* **230**, 583–646.

KOMORI, S. & UEDA, H. 1985 The large-scale coherent structure in the intermittent region of the self-preserving round free jet. *J. Fluid Mech.* **152**, 337–359.

KOOCHESFAHANI, M. M. & DIMOTAKIS, P. E. 1986 Mixing and chemical reactions in a turbulent liquid mixing layer. *J. Fluid Mech.* **170**, 83–112.

LEE, M. & REYNOLDS, W. C. 1985 Bifurcating and blooming jets. *HTTM Rep.* TF–22, Mechanical Engineering Department, Stanford University.

LORENSEN, W. E. & CLINE, H. E. 1987 Marching cubes: A high resolution 3D surface construction algorithm. *Comput. Graphics* **21**, 163–169.

MARTIN, J. E. 1991 Numerical investigation of three-dimensionally evolving jets. Ph.D. thesis, Brown University.

MATTINGLY, G. E. & CHANG, C. C. 1974 Unstable waves on an axisymmetric jet column. *J. Fluid Mech.* **65**, 541–560.

MENDENHALL, W., SCHEAFFER, R. L. & WACKERLY, D. D. 1986 *Mathematical Statistics with Applications.* Duxbury Press.

MICHALKE, A. 1971 Instabilität eines runden Freistrahls unter Berücksichtigung des Einflusses der Strahlgrenzschichtdicke. *Z. Flugwiss.* **19**, 319–328 [English translation: Instability of compressible circular free jet with consideration of the influence of the jet boundary layer thickness. *NASA Tech. Memo No.* 75190, 1977].

MUNGAL, M. G., LOZANO, A. & CRUYNINGEN, I. VAN 1992 Large-scale dynamics in high Reynolds number jets and jet flames. *Exp. Fluids* **12**, 141–150.

MUNGAL, M. G. & O'NEIL, J. M. 1989 Visual observations of a turbulent diffusion flame. *Combust. Flame* **78**, 377–389.

NING, P. C. & HESSELINK, L. 1991 Adaptive isosurface generation in a distortion-rate framework. In *Extracting Meaning from Complex Data: Processing, Display, Interaction II*, SPIE Proc. **1459**, 11–21.

PAPANICOLAU, P. N. & LIST, E. J. 1988 Investigations of round vertical turbulent buoyant jets. *J. Fluid Mech.* **195**, 341–391.

PAPANTONIOU, D. & LIST, E. J. 1989 Large-scale structure in the far field of buoyant jets. *J. Fluid Mech.* **209**, 151–190.

PAREKH, D., LEONARD, A. & REYNOLDS, W. C. 1988 Bifurcating jets at high Reynolds numbers. *HTTM Rep.* TF–35, Department of Mechanical Engineering, Stanford University.

PETERSEN, R. A., SAMET, M. M. & LONG, T. A. 1988 Excitation of azimuthal modes in an axisymmetric jet. In *Turbulence Management and Relaminarisation* (ed. H. W. Liepmann and R. Narasimha), pp. 435–443. Springer-Verlag.

PRASAD, R. R. & SREENIVASAN, K. R. 1990 Quantitative three-dimensional imaging and the structure of passive scalar fields in fully turbulent flows. *J. Fluid Mech.* **216**, 1–34.

RUETSCH G. R. & MAXEY, M. R. 1991 Small-scale features of vorticity and passive scalar fields in homogeneous isotropic turbulence. *Phys. Fluids* A **3**, 1587–1597.

SCHATZLE, P. R. 1987 An experimental study of fusion of vortex rings. Ph.D. thesis, California Institute of Technology.

SHLIEN, D. J. 1987 Observations of dispersion of entrained fluid in the self-preserving region of a turbulent jet. *J. Fluid Mech.* **183**, 163–173.

SONDERGAARD, R., CHEN, J., SORIA, J. & CANTWELL, B. 1991 Local topology of small scale motions in turbulent shear flows. In *Proc. Eighth Symposium on Turbulent Shear Flows, Munich, Germany.*

SORIA, J., CHONG, M. S., SONDERGAARD, R., PERRY, A. E. & CANTWELL, B. J. 1994 A study of the fine scale motions of incompressible time-developing mixing layers. *Phys. Fluids* **6**, 871–884.

STRANGE, P. J. R. & CRIGHTON, D. G. 1983 Spinning modes on axisymmetric jets. Part 1. *J. Fluid Mech.* **134**, 231–245.

TSO, J. & HUSSAIN, F. 1989 Organized motions in a fully developed turbulent axisymmetric jet. *J. Fluid Mech.* **203**, 425–448.

TURNER, J. S. 1966 Jets and plumes with negative or reversing buoyancy. *J. Fluid Mech.* **26**, 779–792.

YODA, M. 1992 The instantaneous concentration field in the self-similar region of a high Schmidt number jet. Ph.D. thesis, Stanford University.

YODA, M., HESSELINK, L. & MUNGAL, M. G. 1992 The evolution and nature of large-scale structures in the turbulent jet. *Phys. Fluids* A **4** 803–811.